

# Robust time-domain full waveform inversion with normalized zero-lag cross-correlation objective function

Youshan Liu,<sup>1</sup> Jiwen Teng,<sup>1</sup> Tao Xu,<sup>1,2</sup> Yanghua Wang,<sup>3</sup> Qinya Liu<sup>4</sup> and José Badal<sup>5</sup>

<sup>1</sup>State Key Laboratory of Lithospheric Evolution, Institute of Geology and Geophysics, Chinese Academy of Sciences, Beijing 100029, China.

E-mail: [ysliu@mail.iggcas.ac.cn](mailto:ysliu@mail.iggcas.ac.cn)

<sup>2</sup>CAS Center for Excellence in Tibetan Plateau Earth Sciences, Beijing 100101, China

<sup>3</sup>Department of Earth Science and Engineering, Imperial College London, SW7 2AZ, United Kingdom

<sup>4</sup>Department of Physics & Department of Earth Sciences, University of Toronto, Toronto, M5S 1A7, Ontario, Canada

<sup>5</sup>Physics of the Earth, Sciences B, University of Zaragoza, Pedro Cerbuna 12, E-50009 Zaragoza, Spain

Accepted 2016 December 22. Received 2016 December 20; in original form 2016 December 13

## SUMMARY

In full waveform inversion (FWI) with the least-squares (L2) norm, the direct amplitude matching is never perfect and the accurate estimation of the seismic source strength is not always available. In contrast, the normalized zero-lag cross-correlation objective function relaxes on the amplitude constraints and emphasizes the phase information when measuring the closeness between the simulated and observed data. This FWI method becomes insensitive to differences in amplitude. Based on this property, we investigate the effectiveness and robustness of FWI with the normalized zero-lag cross-correlation function (CFWI) against the noise and unpredictable amplitude of the data that cannot be modelled by the wavefield extrapolation operator. The effectiveness is firstly tested by noise-free data and data contaminated by Gaussian white noise. In addition, CFWI can invert the data set with incorrect source strength when compared with the L2 norm. Moreover, the data set with incorrect source signature illustrates that CFWI is slightly more insensitive to the error in source signature than the L2 norm. However, a source inversion is still needed when the source signature is severely erroneous. With non-Gaussian noise data, such as contaminated by strong ground motion noise and even by spike-type noise, CFWI provides a comparable result with that of the robust Huber norm. Numerical experiments with non-Gaussian noise also indicate that CFWI can suppress noise in data to produce clearer images when compared with the Huber norm. Besides, CFWI is free of the threshold criterion that controls the transition between the L2 and L1 norms used with the Huber and Hybrid norms and therefore free from tedious trial-and-error tests. Several numerical examples support that CFWI is an alternative and reliable inversion method. However, a numerical test with a 1-D initial model confirms that CFWI is more sensitive to the cycle-skipping problem caused by less-accurate initial velocity model than the L2 norm, which is due to the wrong matched events contributing to spurious local minima of the objective function of CFWI, but to an increase in the objective function used with the L2 norm.

**Key words:** Inverse theory; Waveform inversion; Seismology.

## 1 INTRODUCTION

Seismic waveform tomography or full waveform inversion (FWI) utilizes the full waveform as the data to be fitted by implementing the adjoint-state methods (Lailly 1983; Tarantola 1984; Tromp *et al.* 2005; Liu & Tromp 2006, 2008; Plessix 2006; Chen *et al.* 2007; Tape *et al.* 2009; Liu & Gu 2012). FWI minimizes an objective function that is defined as the difference between the simulated and observed data. It updates the target velocity model iteratively, starting from an appropriate initial model, and eventually enables to extract high-resolution information on the properties of the medium from complete wavefield records. FWI provides not only a

high-resolution geometric picture of the target structures but also quantitative inference of the physical properties (e.g. velocity, density, or/and impedance, etc.) of the subsurface (Mora 1987; Pratt 1990; Pratt & Gouly 1991; Pratt *et al.* 1996, 1998; Operto *et al.* 2007; Wang & Rao 2009). However, despite its great potential, FWI suffers from drawbacks such as non-linearity and ill-posed inversion problem, besides its high computational cost (Wang & Rao 2006).

Mathematically, FWI is a non-linear optimization problem. Although the global optimization methods, such as the Monte Carlo-based inversion methods (Rothman 1985; Kvoren *et al.* 1991; Mosegaard & Tarantola 1995), tend to search for a global optimal solution, the expensive cost required for its convergence makes

these methods beyond ordinary computational capabilities. In practice, the local optimization methods represent a feasible way to deal with this issue. The presence of cycle-skipping associated with the high-frequency waveforms, the sinusoidal nature of the seismic wavefields and the complexity of the earth reflectivity are responsible for spurious local minima (Sirgue & Pratt 2004; Plessix *et al.* 2010; ten Kroode *et al.* 2013). A successful inversion performed with the help of gradient-based FWI requires that the misfit function produced by an initial velocity model is located within the basin of attraction of the global minima of the objective function. Generally, both the width of this basin of attraction and the length of the half-cycle increase at low frequencies and large offsets (Sirgue & Pratt 2004). Unfortunately, sufficiently low frequencies as well as large enough offsets are not available from real data. Some efforts have been undertaken to overcome this problem, such as multiscale strategy (Bunks *et al.* 1995; Ravaut *et al.* 2004; Fichtner *et al.* 2008, 2013; Liu *et al.* 2017), early arrival waveform method (Sheng *et al.* 2006), exponential time-damping scheme (Brenders *et al.* 2009), time or/and offset window method (Kurzmann 2012; Shipp & Singh 2002), and Laplace-domain FWI (Shin & Cha 2008; Shin & Ha 2008). A reliable choice is the combination of FWI with traveltime tomography, so that the output model provided by tomography is then used as the input model for FWI. Although this procedure is robust, it requires an arduous task of seismic phase identification and tedious traveltime picking.

In the context of FWI, the topology in the solution space is closely related to the adopted objective function (Fichtner 2010; Bulcão *et al.* 2013; Jimenez Tejero *et al.* 2014). Because different parts of seismic data (such as traveltime, amplitude, phase, etc.) have different sensitivity to the inversion, they have different behaviour (Wang & Pratt 1997). In particular, some objective functions may give rise to good performance and at the same time to be robust, what is really necessary especially for noisy data. Many objective functions have been proposed to date. Luo & Schuster (1991) constructed the cross-correlation traveltimes between the simulated and observed waveforms to obtain an objective function with more linear behaviour with respect to the velocity model. Although this objective function is insensitive to cycle-skipping problems, it is sensitive to the differences in amplitude spectra and does not allow addressing multi-arrival problems easily (Hörmann & de Hoop 2002; de Hoop & van der Hilst 2005). Later, van Leeuwen & Mulder (2010) used a weighted norm of the cross-correlation that is insensitive to the differences in amplitude spectra. Also, a dynamic image warping method of seismic images was proposed to handle multi-arrivals data (Hale 2013). In an attempt to evolve towards the exploitation of the full wavefield, Fichtner *et al.* (2008) and Bozdag *et al.* (2011) proposed misfit functions based on both the phase and amplitude attributes. FWI based on envelope objective function has been also proposed to mitigate the absence of low frequency data because the envelope of seismic data contains abundant low frequency information (Chi *et al.* 2014; Wu *et al.* 2014; Luo & Wu 2015). Usually, waveform inversion through the phase approach tends to make the misfit function be more linear (Kim & Shin 2005; Shin & Min 2006; Bednar *et al.* 2007). On this issue, Alkhalifah & Choi (2014) proposed an unwrapped phase estimation method that is easy to use and quantify. Compared to the conventional phase representation, the unwrapped phase estimation helps to reduce the non-linearity of the inversion.

In practice, data is always contaminated by stochastic or/and coherent noise, which further aggravates the non-linearity and difficulty of FWI (Wang & Rao 2006). Since the direct amplitude matching of the least-squares (L2) norm is never perfect, it is desirable an

objective function with robust performance to deal with this kind of data. To address this problem, some authors have proposed several objective functions (Djikpéssé & Tarantola 1999; Guitton & Symes 2003; Brossier *et al.* 2009, 2010; Ha *et al.* 2009; Pyun *et al.* 2009; Bulcão *et al.* 2013; Jimenez Tejero *et al.* 2014). The Huber function (Huber 1973) is highlighted as the most robust norm among all of them. The L2 norm is always highly sensitive to non-Gaussian noise facing the reconstruction of models. The least-absolute-value (L1) norm shows a more robust behaviour whatever the noise characteristics, which allows the convergence towards admissible models (Brossier *et al.* 2009). Although the L1 norm is more robust to noise than the L2 norm, the gradient of the L1 norm presents a singularity when the residuals vanish. Then the Huber function adopts the L1 norm when residuals are large and the L2 norm when residuals are small, thus overcoming such singularity problem. The robustness of FWI with the Huber norm has been verified by Guitton & Symes (2003) and Ha *et al.* (2009). The study carried out by Brossier *et al.* (2010) proved that the L1 norm provides the most reliable models even with strongly decimated data sets, while the L2 norm can provide reliable results in the presence of uniform white noise. Although the Huber and Hybrid norms (Bube & Langan 1997) allow obtaining models when working with noisy data, both norms are sensitive to a threshold criterion (Brossier *et al.* 2010) that controls the transition between the L1 and L2 norms. Tedious trial-and-error tests are required for reliable estimation with the Huber and Hybrid norms (Brossier *et al.* 2010).

To overcome the problem of the imperfect amplitude matching in real circumstance, in this study, we adopt the normalized zero-lag cross-correlation objective function for FWI. Routh *et al.* (2011a,b) and Choi & Alkhalifah (2012) suggested this objective function for the application of encoded multisource full waveform inversion to adapt to non-fixed marine streamer data. Also, it has also been used in least-squares reverse time migration (Zhang *et al.* 2013, 2015), revealing itself as a stable and practical method. Dutta *et al.* (2014) proved that this objective function is also an alternative solution to visco-acoustic least-squares migration when there is strong attenuation in the subsurface and the estimation of the attenuation parameter is insufficiently accurate (Dutta *et al.* 2014). Given that this function maximizes the minus value of the normalized zero-lag cross-correlation rather than differences in amplitude, it relaxes on the amplitude matching and uses the phase information to measure the closeness between the simulated and observed seismic data, so that the differences in amplitude contribute less than the differences in phase (Zhang *et al.* 2015). In the best scenario, in which the two data sets are identical or with a constant scaling difference, the objective function reaches its minimum  $-1$ . In practice, the source strength always varies from one to another source and its accurate estimation is difficult. Now, since the normalized zero-lag cross-correlation objective function is insensitive to the differences in source strength facing the simulated and observed data, it is free of the estimation of source strength.

Although the normalized zero-lag cross-correlation function for FWI has been used before, its robustness to non-Gaussian noise, insensitivity to source signature, and sensitivity to the cycle-skipping problem, never have been systematically investigated to date. In this study, we investigate the behaviour of FWI with this function with respect to these issues using a 2-D canonical model. Then, we systematically investigate the effectiveness and robustness of FWI with this function using both noise-free data and Gaussian white noise data. We also study the problem raised by differences in amplitude of the data as a consequence of the variable seismic source strength. We use noise-free data generated by incorrect source wavelet to test

its sensitivity to source signature. In order to check the robustness and stability of the process, we compare it with the L2 norm and Huber norm for inversion using non-Gaussian noise data. We also consider a 1-D model to verify the sensitivity of FWI with this function to cycle-skipping caused by less-accurate initial model.

## 2 NORMALIZED ZERO-LAG CROSS-CORRELATION-BASED FULL WAVEFORM INVERSION

Essentially, FWI aims to find a velocity model that allows us to interpret the available data correctly. This process is carried out by calculating synthetic seismic records from a previously assumed model with the purpose of comparing with the observed data. If the fit is not acceptable, the model is updated so that the synthetic data are regenerated, and the procedure is repeated until the convergence is achieved. It is a powerful technique in seeking images and properties (such as velocity and impedance) of complex geological structures. The important criterion to measure the error between the simulated (or predicted) and observed data is an objective function.

The standard implementation of FWI relies on the use of the L2 norm as the objective function that expresses the difference between the simulated and observed data. The L2 norm strongly emphasizes the matching of the amplitudes between the simulated and observed data. However, with real data, it is not easy to match the amplitudes directly because of several factors. First, the real earth is viscoelastic so that the amplitudes and phases of the propagating seismic waves are severely distorted (Dutta *et al.* 2014). As a result, the resolution of the inverted models decreases (Causse *et al.* 1999). Although viscoelastic simulations can mitigate this issue, it is computationally expensive. In addition, the estimation of the attenuation parameter is really difficult. Second, it is difficult to obtain a good estimation of the source signature and indeed the source strength varies at different shot locations.

Here, we consider full waveform inversion with the normalized zero-lag cross-correlation function (i.e. correlative full waveform inversion, hereafter CFWI). This function can be written as

$$E(c) = -\frac{1}{N_s N_r} \sum_s \sum_r \frac{\int d(\mathbf{x}_r; t; \mathbf{x}_s; c) \cdot D(\mathbf{x}_r; t; \mathbf{x}_s) dt}{\sqrt{\int d(\mathbf{x}_r; t; \mathbf{x}_s; c)^2 dt} \sqrt{\int D(\mathbf{x}_r; t; \mathbf{x}_s)^2 dt}}, \quad (1)$$

where  $c$  is the velocity model;  $N_s$  and  $N_r$  represent the number of shots and receivers, respectively;  $d(\mathbf{x}_r; t; \mathbf{x}_s; c)$  and  $D(\mathbf{x}_r; t; \mathbf{x}_s)$  are the simulated and observed data at the receiver  $\mathbf{x}_r$  and the time instant  $t$ , respectively, which are excited by a source located at position  $\mathbf{x}_s$ . The summation is performed over sources (subscript  $s$ ) and receivers (subscript  $r$ ). The negative sign on the right-hand side means that the minus value of the normalized zero-lag cross-correlation function is minimized or the normalized zero-lag cross-correlation function itself is maximized. Since this function measures the similarity between the simulated and observed data, it relaxes on the amplitude adjustment criterion required by the L2 norm and emphasizes the phase-mismatch. This objective function is equivalent to a time-domain phase inversion method where the phase spectra of the simulated data are matched with those of the observed data (Schuster 1991; Sun & Schuster 1993; Routh *et al.* 2011a,b; Zhang *et al.* 2013; Dutta *et al.* 2014). Thus, it reduces the importance of the amplitude and provides the basis for using the phase information to measure the closeness between the observed and simulated seismic data. Therefore, it encloses high expectations to be insensitive to

noise and unpredicted data that cannot be modelled by the wavefield extrapolation operator.

After defining the objective function, the core part of the gradient-based FWI algorithm that enables us to solve the non-linear optimization problem (1) is the computation of the gradient function. Because a change of the objective function only changes the adjoint source but not the whole gradient expression, CFWI has formally the same gradient expression as for the L2 norm (Cruse *et al.* 1990). In the context of the adjoint-state method and acoustic media, the gradient of the objective function (1) with respect to the velocity model  $c$  is calculated by the zero-lag cross-correlation between forward-propagated wavefields and backward-projected wavefield residuals (Tarantola 1984; Boonyasiriwat *et al.* 2009)

$$g(\mathbf{x}) = \frac{2}{c(\mathbf{x})} \sum_s \int \frac{\partial^2}{\partial t^2} p(\mathbf{x}; t; \mathbf{x}_s) \cdot q(\mathbf{x}; t; \mathbf{x}_s) dt, \quad (2)$$

where the adjoint wavefield  $q(\mathbf{x}; t; \mathbf{x}_s)$  is generated by back-propagating the following residuals,

$$\Delta d = \frac{1}{\sqrt{\int D^2 dt} \sqrt{\int d^2 dt}} \left( \frac{\int d \cdot D dt}{\int d^2 dt} d - D \right), \quad (3)$$

where  $d$  denotes the simulated data and  $D$  the observed data. Here,  $\frac{\int d \cdot D dt}{\int d^2 dt} d$  represents the rescaled simulated data used to correct the amplitude differences between the observed and simulated data. The weight before the square brackets aims to remove the amplitude strength effects derived from the observed and simulated data. For this reason, CFWI is free from an accurate estimation of the source strength since the differences in amplitude between the observed and simulated seismic data are normalized by the reweighted residuals (3). It can be seen that the computation of the gradient (2) involves twice wavefield extrapolation. In this study, we adopt a central finite-difference stencil of the 16th-order accuracy in space and the second-order accuracy in time to extrapolate the source wavefield and the receiver wavefield. We solve the second-order acoustic wave equation considering perfectly matched layers as absorbing boundary conditions (Liu *et al.* 2012) to suppress spurious reflections from the four artificial boundaries.

Once the gradient is formulated, we need to select a practical inversion method to solve the non-linear optimization problem (1). Although some global optimization methods based on a random sampling of the model-space can be theoretically feasible, these methods generally require many expensive evaluations of the misfit function for each new model (Rothman 1985; Kvoren *et al.* 1991; Guitten 2012), which is a long and costly process. In practice, the local optimization methods are usually preferred in terms of computational efficiency although they are inherently limited to local convergence and cannot guarantee a global solution, unless the misfit produced by an initial velocity model locates within the basin of attraction of the global minima of the objective function (Pratt *et al.* 1998). For this reason, we adopt the Limited-memory Broyden–Fletcher–Goldfarb–Shanno (L-BFGS) method as our inversion method (Nocedal 1980), such as Liu *et al.* (2017) have applied recently. The step-length for implementation is calculated by the parabolic searching method (Vigh *et al.* 2009), such as Liu *et al.* (2017) have applied recently.

In order to measure the accuracy (error) of the inverted results, we use the following mean absolute percentage error (MAPE)

$$\varepsilon = \frac{100}{N} \sum \left| \frac{c_{true} - c_{inv}}{c_{true}} \right|, \quad (4)$$

where  $N$  is the total number of grids of the discretized model, and  $||$  represents the absolute operator. The smaller the MAPE, the more accurate the inverted result. In the next sections, we investigate the effectiveness, sensitivity and robustness of CFWI.

### 3 BEHAVIOURS OF THE L2 NORM AND THE NORMALIZED ZERO-LAG CROSS-CORRELATION FUNCTION

In order to test the behaviours of the objective functionals such as the L2 norm and the normalized zero-lag cross-correlation function in seismic waveform inversion (Jimenez Tejero *et al.* 2014), we consider a 2-D canonical model as shown in Fig. 1 to investigate their respective sensitivities to cycle-skipping, source signature and noise. The discretized model consists of  $301 \times 101$  grid-cells in both horizontal and vertical directions. Both the horizontal and vertical grid spacing is 5 m. We adopted a fixed-spread geometry with 16 sources and 301 receivers evenly located on surface. The seismic source is modelled by a Ricker wavelet whose dominant frequency is 15 Hz. The real velocity model is a medium with a 1-D background velocity gradient, in which the velocity increases vertically from  $1.5 \text{ km s}^{-1}$  at the surface to  $4.5 \text{ km s}^{-1}$  at the bottom, together with a buried spherical-shaped body (circle in the plane) with a radius of 0.1 km and seismic velocity of  $v_0 = 5.0 \text{ km s}^{-1}$  (Fig. 1). A certain number of initial velocity models are generated and inverted at once to investigate the sensitivity of FWI with the L2 norm and the normalized zero-lag cross-correlation function to the above mentioned three factors. In all these artificially generated initial velocity models, the background velocity is controlled by two parameters: its value  $v_0$  assigned to the spherical-shaped body and the value  $v_2$  at the bottom. In addition, the value  $v_1$  at the surface is fixed to  $1.5 \text{ km s}^{-1}$ . These initial velocity models are constructed in the following manner:  $v_2$  varies widely from 1.5 to  $7.5 \text{ km s}^{-1}$  with velocity interval of  $0.1 \text{ km s}^{-1}$ , while the value  $v_0$  assigned to the buried body varies from 2.0 to  $7.0 \text{ km s}^{-1}$  with the same velocity interval.

In this numerical experiment, we consider three data sets: noise-free data simulated by the true source wavelet, noise-free data simulated by a severely incorrect source wavelet, and noisy data. Fig. 2 shows the true source wavelet and two incorrect source wavelets (labelled I and II in the illustration) in time-domain (a) and frequency-domain (b). The first incorrect source wavelet presents large side lobes and deviates far from the true source wavelet, while the second incorrect source wavelet is closer to the true source wavelet with the

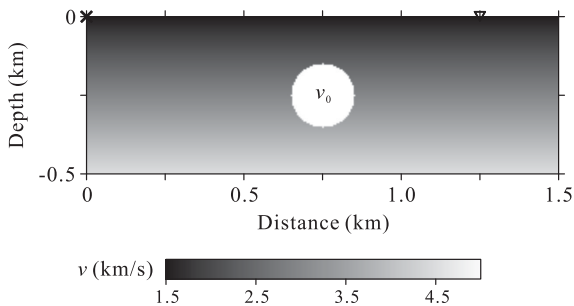


**Figure 1.** A 2-D canonical model integrated by a medium where the velocity increases vertically from  $1.5 \text{ km s}^{-1}$  at surface to  $4.5 \text{ km s}^{-1}$  at the bottom, and a buried spherical-shaped body (circular in the plane) that has a radius of 0.15 km and seismic velocity  $v_0 = 5.0 \text{ km s}^{-1}$ . On top, the cross denotes the first shot point, while the triangle denotes a receiver.

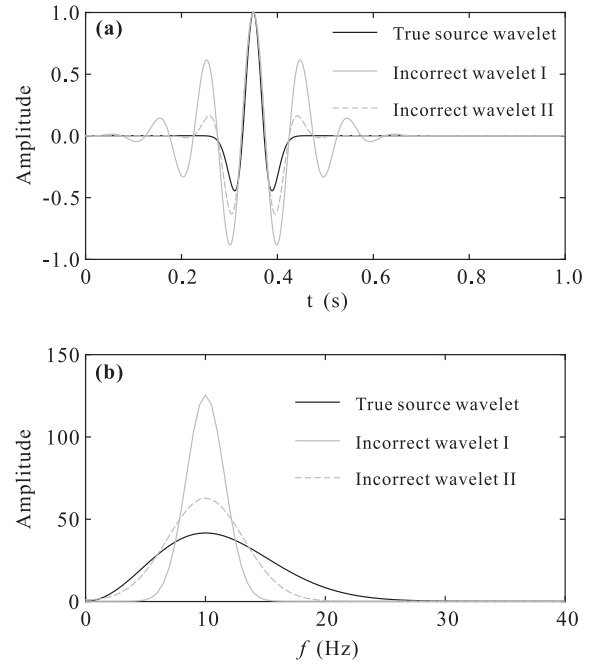
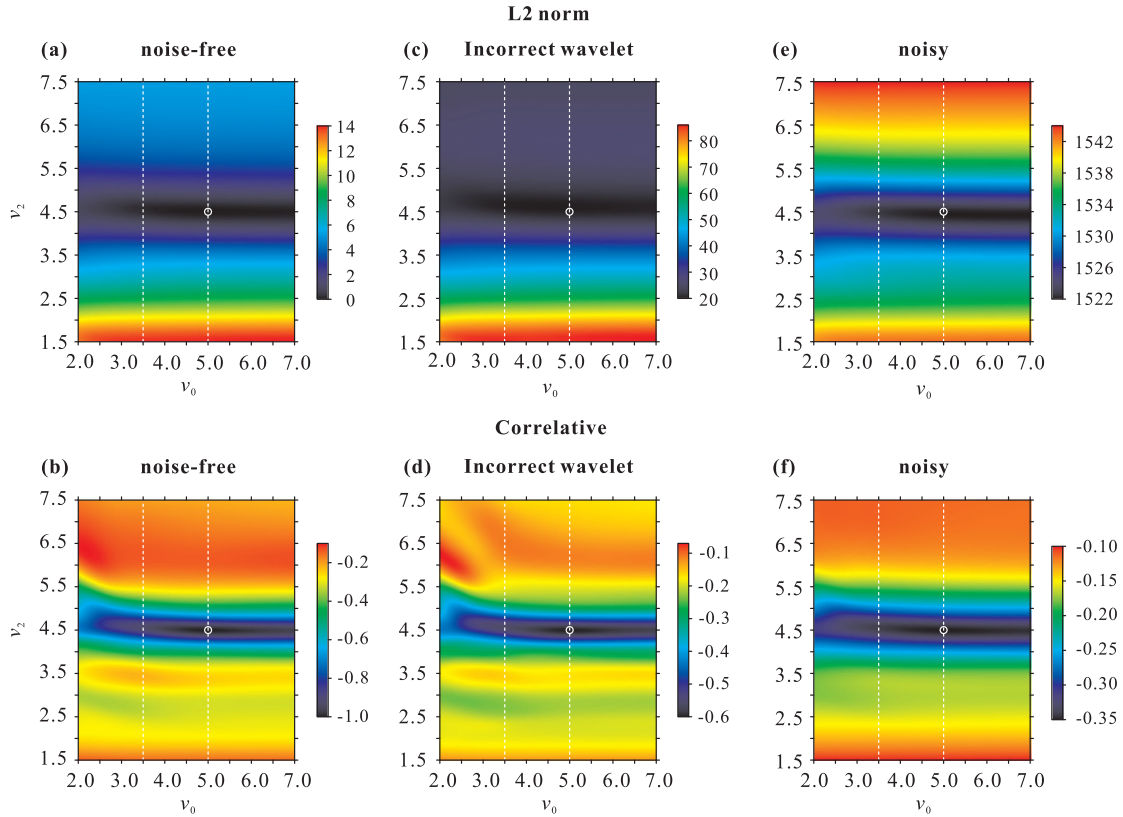


**Figure 2.** Source wavelets in time-domain (a) and frequency domain (b). The solid black lines represent the true wavelet, while the solid and dashed grey lines represent the two incorrect source wavelets, respectively.

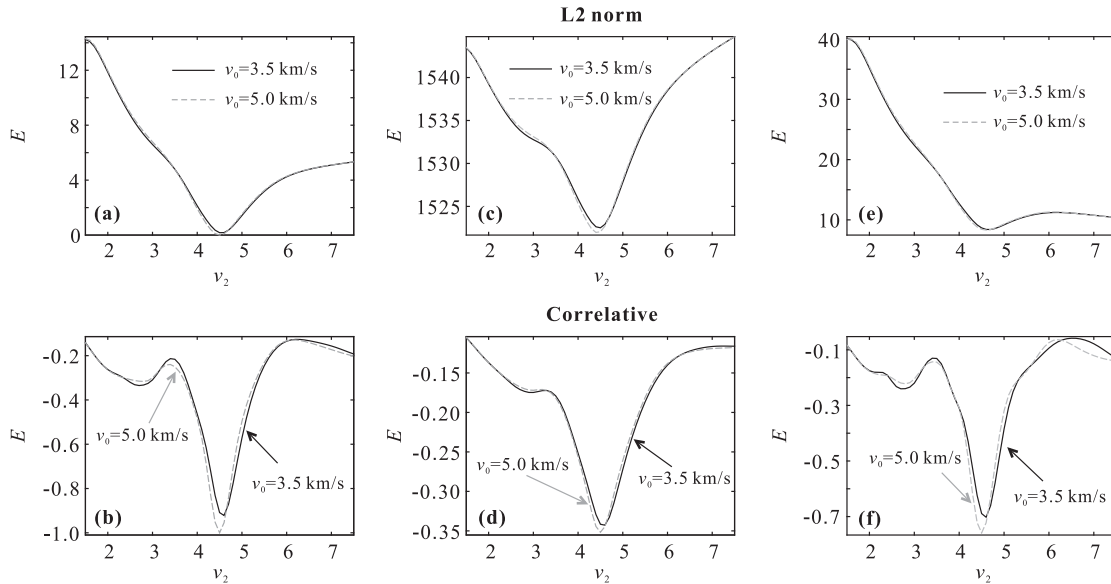
exception of two smaller side lobes. In this experiment, we adopt the first incorrect source wavelet. The noisy data (the third data set) are generated by adding Gaussian white noise to the noise-free data to obtain a signal-to-noise ratio (SNR) of 20 dB, and then some seismic traces are rescaled by a factor 20 to simulate non-Gaussian noise.

Fig. 3 shows the misfit function values obtained with the L2 norm (top) and the normalized zero-lag cross-correlation function (bottom): panels (a) and (b) show these values with the noise-free data simulated by the true source wavelet; panels (c) and (d) show these values with the noise-free data simulated by the first incorrect source wavelet shown in Fig. 2; and panels (e) and (f) show these values with the non-Gaussian noise data. In the three cases, it can be seen that the two objective functions are really sensitive to the velocity value  $v_2$  at the bottom of the model (vertical axes) and insensitive to the velocity value  $v_0$  assigned to the spherical-shaped body (horizontal axes). For the noise-free data simulated by the first incorrect source wavelet, the global minimum given by the L2 norm (marked by a white circle in Fig. 3c) becomes narrower than that obtained from the noise-free data simulated with true source wavelet (Fig. 3a), while the normalized zero-lag cross-correlation function suffers a less impact (Fig. 3d) although a higher sensitivity to the value  $v_0$ . For the noisy data (Fig. 2e), the width of the global minimum using the L2 norm is quite similar to that of the minimum obtained from the noise-free data (Fig. 3a). In contrast, the normalized zero-lag cross-correlation function seems to be less sensitive to non-Gaussian noise (Fig. 3f) and always has a narrower global minimum, issue on which we will return in Section 4.5.

This can be seen with clarity in Fig. 4 where for each individual experiment we have extracted two curves from Fig. 3 when the velocity values for the spherical-shaped body are  $v_0 = 3.5 \text{ km s}^{-1}$  (solid black lines) and  $v_0 = 5.0 \text{ km s}^{-1}$  (dashed grey lines), respectively. In all cases, it can be observed that the width of



**Figure 3.** Values of the misfit function ( $E$ ) depending on a series of initial velocity models, all of them with the geometry of the model shown in Fig. 1, and characterized by a vertically varying background velocity, from  $1.5 \text{ km s}^{-1}$  at surface to  $7.5 \text{ km s}^{-1}$  at the bottom (vertical axis), together with an embedded spherical-shaped body in which the velocity varies from  $2.0$  to  $7.0 \text{ km s}^{-1}$  (horizontal axis). Panels (a) and (b) represent the misfit functions obtained with the L2 norm and the normalized zero-lag cross-correlation function from noise-free data simulated by the true source wavelet, respectively. Panels (c) and (d) show these same functions computed with noise-free data simulated by the incorrect source wavelet I (shown in Fig. 2). Panels (e) and (f) show these same functions computed with data contaminated by non-Gaussian noise. The dashed white lines represent two cuts for velocity values  $v_0 = 3.5 \text{ km s}^{-1}$  and  $v_0 = 5.0 \text{ km s}^{-1}$  of the spherical body. The white circles represent the global minimum.



**Figure 4.** Curves extracted from the panels shown in Fig. 3 by following the dashed white lines corresponding to the velocity value  $v_0 = 3.5$  (solid black lines) and  $v_0 = 5.0$  (dashed grey lines)  $\text{km s}^{-1}$  of the spherical-shaped body, respectively. Panels (a) and (b) show the value of the misfit functions ( $E$ ) calculated with the L2 norm (top) and the normalized zero-lag cross-correlation function (bottom), respectively, from noise-free data simulated by the true source wavelet. Panels (c) and (d) show the same functions computed for noise-free data simulated by the incorrect source wavelet I (shown in Fig. 2), respectively. Panels (e) and (f) show such functions for non-Gaussian noise data, respectively.

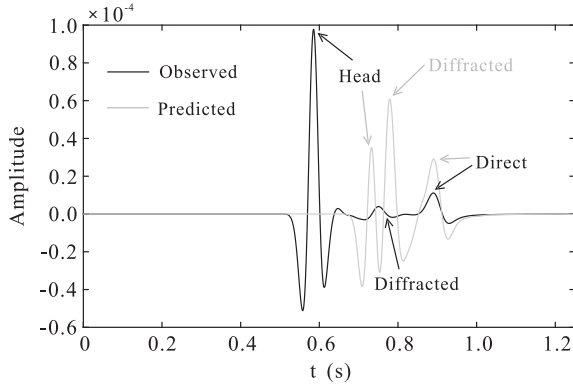


**Figure 5.** The observed (solid black line) and predicted data (dashed grey line) excited by the first shot shown in Fig. 1 and recorded at the receiver (the triangle). The head, diffracted and direct waves are indicated.

the basin of attraction of the global minimum obtained with the normalized zero-lag cross-correlation function is significantly narrower than that the width obtained with the L2 norm. For the noise-free data simulated by the first incorrect source wavelet, the L2 norm gives a local maximum at about the point  $v_2 = 6.0 \text{ km s}^{-1}$  (Fig. 4c), which decreases the width of the basin of attraction of the global minimum. For the noisy data, the L2 norm has a potential local minimum (an inflection point) at about the point  $v_2 = 2.8 \text{ km s}^{-1}$  (Fig. 4e). Unlike the L2 norm, the misfit function value deduced with the normalized zero-lag cross-correlation function always has a global minimum within a narrower attraction basin and exhibits a spurious local minimum at about the point  $v_2 = 2.9 \text{ km s}^{-1}$  that does not appear with the L2 norm (Figs 4b, d, and f).

In order to find out the reason for this local minimum, in Fig. 5 we plotted the observed and predicted data on surface at distance of 1.25 km (the inverted triangle in Fig. 1) far from the first shot point (the cross in Fig. 1). Obviously, the predicted head wave does not match with the observed head wave but wrongly match with the observed diffracted wave produced by the buried body, which leads to the predicted data generated by this initial model (at about the point  $v_2 = 2.9 \text{ km s}^{-1}$ ) to suffer a cycle-skipping problem (i.e. the starting model generates predicted data that differ from the observed data by more than half a cycle). As the L2 norm mainly measures the amplitude mismatch, this amplitude difference leads to an increase in the L2 norm objective function. In contrast, the normalized zero-lag cross-correlation emphasizes the phase-mismatch, so that the two upward peaks (calculated head wave and observed diffracted wave in Fig. 5) produce an increase in the normalized zero-lag cross-correlation coefficient, that is a decrease in the objective function (in the minus value of the normalized zero-lag cross-correlation coefficient). This confirms that the normalized zero-lag cross-correlation function seems to be more sensitive to the cycle-skipping problem caused by less-accurate initial model. This issue will be further discussed later in Section 5. As pointed by Warner & Guasch (2016), such a cycle-skipped model represents a spurious local minimum of the conventional FWI objective function, so that a perturbation of the model in any direction will worsen the fit to the observed data even it may improve the fit to the true model. Therefore, the cycle-skipping problem increases the chance of CFWI convergence to local minima.

## 4 EFFECTIVENESS AND ROBUSTNESS OF CFWI

### 4.1 Test with noise-free data

To investigate the effectiveness of CFWI, we use the Marmousi velocity model, which is shown in Fig. 6(a) together with two initial models: one is a realistic initial model obtained by the first-arrival traveltime tomography based on the adjoint-state method (Leung & Qian 2006; Taillandier *et al.* 2009; Huang & Belleur 2012; Bretaudeau *et al.* 2014; Daniel Köhn, personal communication, 2016), which is taken as our initial velocity model A (Fig. 6b); the other is a velocity model named B (Fig. 6c) that can generate predicted data being free from the cycle-skipping problem (discussed in Section 5). This latter is a 1-D model whose profile along the  $z$ -axis is shown on the right-hand side of the Fig. 6(c). In this 1-D model, the topmost 0.22 km consist of a water column that has a velocity value of  $1.5 \text{ km s}^{-1}$  (typical velocity of water layers), which overlies other layers whose respective velocities range from 1.5 to  $4.5 \text{ km s}^{-1}$  (this last model will be used in Section 5). The MAPEs in relation to both the initial models A and B are 8.74 and 9.85 per cent, respectively. The true model consists of  $500 \times 174$  grid-cells in the horizontal and vertical directions, respectively. Both the horizontal and vertical grid spacing is 10 m. The synthetic data used as common shot gathers come from 34 shots separated by an interval of 0.15 km and are used as common shot gathers. The seismic source is located at the depth of 0.05 km and is modelled by a Ricker wavelet with dominant frequency of 22 Hz. Up to 500 seismic receivers are evenly deployed on surface with fixed-spread acquisition geometry. The sampling interval is 0.5 ms and the recording length is 3.6 s.

We use the multiscale strategy (Boonyasiriwat *et al.* 2009; Wang 2011; Liu *et al.* 2017) to invert the shot gathers obtained from the Marmousi model. With this strategy, seismic data and Ricker wavelet are decomposed into two frequency bands with the help of a Wiener low-pass filter (Boonyasiriwat *et al.* 2009), namely: [3.1 Hz, 10.6 Hz], and [10.6 Hz, 36.0 Hz]. In all experiments, we apply successively these two frequency bands and the true source wavelet to FWI, unless otherwise noted. Identical stopping criteria are set for FWI with different objective functions: the relative change in the value of the objective function value must be less than 0.0001.

Firstly, we utilize FWI with the L2 norm and the normalized zero-lag cross-correlation function to invert the synthetic data generated with the Marmousi model reproduced in Fig. 6(a). The initial velocity model is the one shown in Fig. 6(b). Fig. 7 shows the common shot gathers for the 17th shot fired at the middle of the model (Fig. 6a), either noise-free (Fig. 7a) or with Gaussian white noise and SNR of 20 dB (Fig. 7b). Fig. 8 shows the multiscale images obtained using the noise-free data (Fig. 7a) and two different objective functions. The left-hand column are the results obtained by the conventional L2 norm at the two frequency bands indicated above (from low to high frequency bands, a and b), while the right-hand column are the results obtained by the normalized zero-lag cross-correlation function at the same two frequency bands (from low to high frequency bands, c and d). By comparing the results at each scale, we can see that both functionals reconstruct the Marmousi model quite well.

The MAPEs related to the inverted results represented in Figs 8(b) and (d) are 4.52 and 3.76 per cent, respectively. Compared with the MAPE related to the initial model A (8.74 per cent), the MAPEs associated with the inverted results reveal a significant decrease that demonstrates the effectiveness of FWI with the normalized

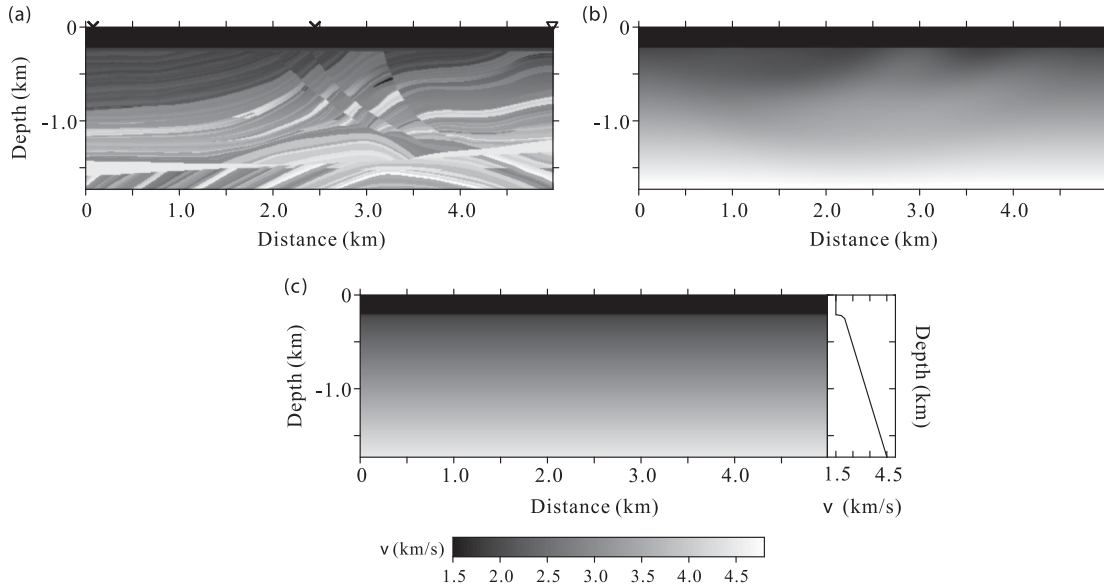


**Figure 6.** The Marmousi model. (a) Real velocity model. (b) A model obtained by the first-arrival traveltome tomography based on the adjoint-state method, which is labelled as initial velocity model A. (c) Initial velocity model B, which is defined as a 1-D velocity model whose profile is shown on the right-hand side. A 0.22-km-thick water layer with the same speed value of  $1.5 \text{ km s}^{-1}$  (typical velocity of water layers) overlies other layers whose velocity values range from  $1.5$  to  $4.5 \text{ km s}^{-1}$  along the depth  $z$ -axis and remain invariable laterally along the horizontal  $x$ -axis. The crosses indicate the positions of first and 17th shot points, while the triangle marks the position of the last receiver.

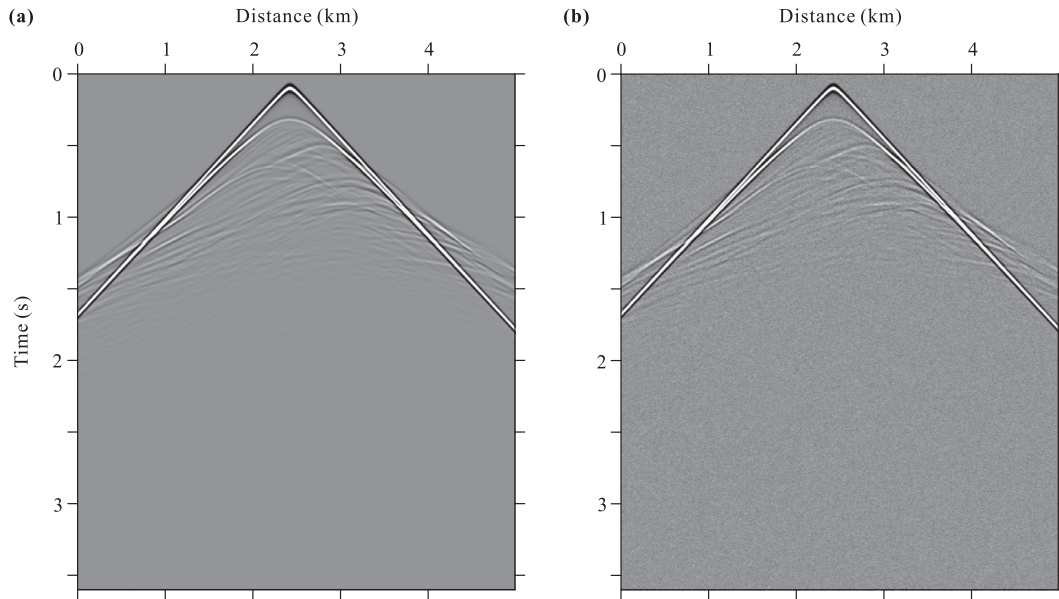


**Figure 7.** Common shot gathers of the 17th shot generated from the Marmousi model, without and with Gaussian white noise: (a) noise-free data; (b) data contaminated by Gaussian white noise with signal-to-noise ratio (SNR) of 20 dB.

zero-lag cross-correlation function. Furthermore, the normalized zero-lag cross-correlation function (MAPE of 3.76 per cent) provides a slightly more accurate result than the L2 norm (MAPE of 4.52 per cent) for this noise-free data.

#### 4.2 Sensitivity of CFWI to Gaussian white noise

Taking advantage of the previously synthesized shot gathers from the Marmousi model reproduced in Fig. 6(a), we now use these shot gathers contaminated by Gaussian white noise being SNR equal to 20 dB. Fig. 7(b) shows the records contaminated by Gaussian white noise for the 17th shot. We invert these shot gathers with the initial

velocity model A and applying the multiscale strategy. The two frequency bands here considered are the previously listed in Section 4.1, that is the frequency bands [3.1 Hz, 10.6 Hz], and [10.6 Hz, 36.0 Hz]. The inverted results obtained with the data contaminated by Gaussian white noise (Fig. 7b) and the two frequency bands are shown in Fig. 9. The left-hand column shows the multiscale images obtained by the conventional L2 norm (from low to high frequency bands, a and b), while the right-hand column shows the results obtained by the normalized zero-lag cross-correlation function at the same two frequency bands (from low to high frequency bands, c and d). Like with the noise-free data, both norms again reconstruct the Marmousi model reasonably well.

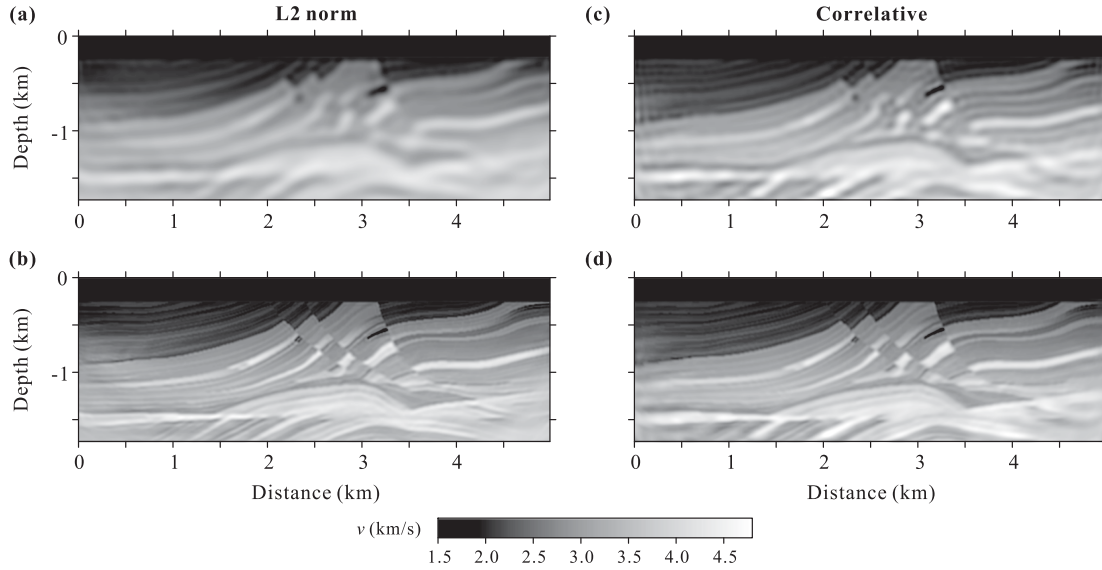


**Figure 8.** Multiscale images obtained using noise-free data (Fig. 7a) and two different objective functions. The initial model is shown in Fig. 6(b). The left-hand column are the results obtained by the conventional L2 norm at two frequency bands (from low to high frequency bands, a and b), while the right-hand column are the results obtained with the normalized zero-lag cross-correlation function at the same frequency bands (from low to high frequency bands, c and d).

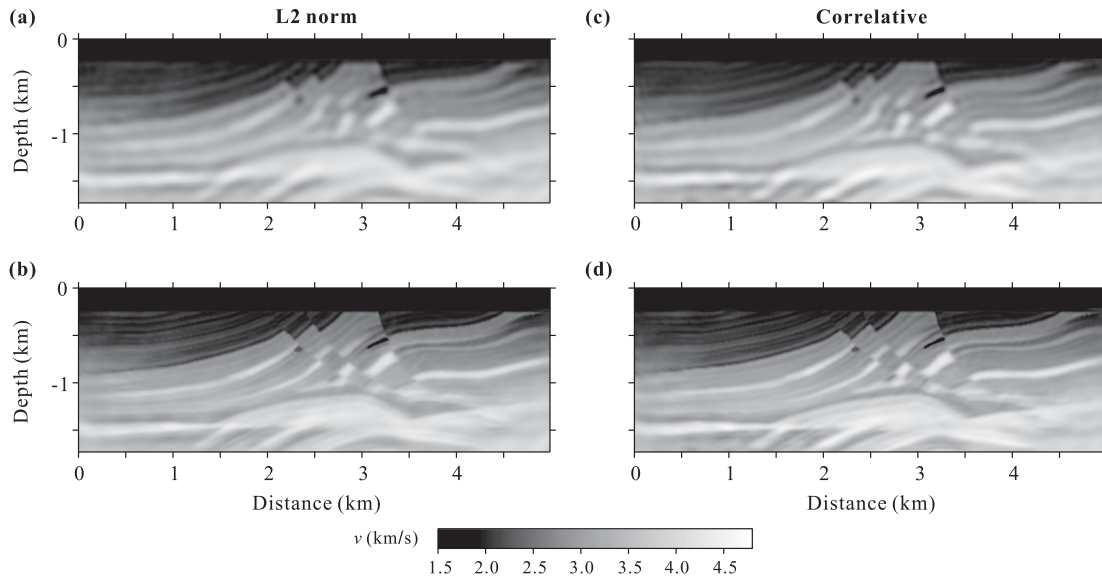


**Figure 9.** Same as in Fig. 8, using the Gaussian white noise data (Fig. 7b).

The MAPEs related to the inverted results shown in Figs 9(b) and (d) are 5.06 and 4.47 per cent, respectively, which are significantly smaller than the MAPE related to the initial model A (8.74 per cent). This proves that both the L2 norm and the normalized zero-lag cross-correlation function are computationally robust with respect to the data contaminated by Gaussian white noise. This conclusion is consistent with the results presented by Brossier *et al.* (2010). Again the normalized zero-lag cross-correlation function provides a slightly more accurate result (MAPE of 4.47 per cent) than the L2 norm (MAPE of 5.06 per cent) for Gaussian noise data. However, the results obtained with the Gaussian white noise data (Fig. 9) generally have lower resolution when compared to those obtained with the noise-free data (Fig. 8).

### 4.3 Sensitivity of CFWI to source strength

As stated above, the normalized zero-lag cross-correlation function is free from an accurate estimation of the source strength because it normalizes the differences in amplitude between the observed and calculated seismic data. For comparison purpose, the shot gathers generated with the Marmousi model (Fig. 7a) are now arbitrarily rescaled to produce new synthetic records simulating different source strengths for each of the 34 shots, although the source strength is identical for the simulated data of all shots. The scalars used for this rescaling operation vary from  $\sim 10^3$  to  $10^5$  for each shot, as listed in Fig. 10. We invert these shot gathers with the initial velocity model A (Fig. 6b) and applying the multiscale strategy. The two frequency bands considered for this strategy are those mentioned above. Similarly, both the noise-free data and Gaussian

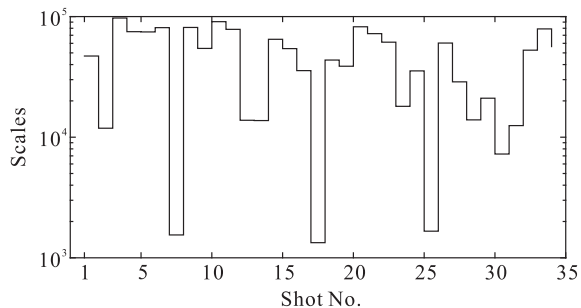


**Figure 10.** Scalars that were used to arbitrarily rescale 34 shot gathers synthesized from the Marmousi model.

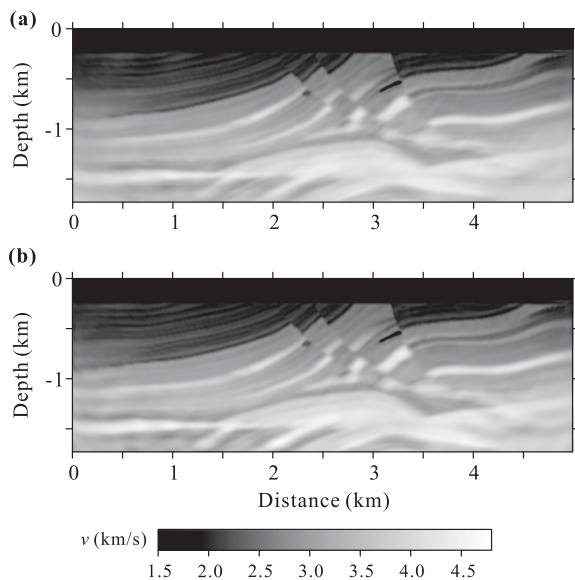


**Figure 11.** Multiscale images obtained using arbitrarily rescaled data (by applying the scalars indicated in Fig. 10) and the normalized zero-lag cross-correlation function. The initial model is shown in Fig. 6(b). Panel (a) is the result obtained with the rescaled noise-free data (reference Fig. 7a). Panel (b) is the result obtained with the rescaled data contaminated by Gaussian white noise with low signal-to-noise ratio (SNR) of 20 dB (reference Fig. 7b).

white noise data are considered again to carry out this numerical experiment.

As expected, FWI with the conventional L2 norm fails to invert this rescaled shot gathers without appropriate data pre-processing (the results are not shown), while FWI with the normalized zero-lag cross-correlation function is able to invert this rescaled shot gathers directly. Fig. 11(a) shows the result obtained by CFWI for the rescaled noise-free data (Fig. 9a), while Fig. 11(b) shows the result with the rescaled data contaminated by Gaussian white noise. The MAPEs related to both results are 4.45 and 4.62 per cent, respectively. After comparing Fig. 11(a) with Fig. 8(d), it is confirmed that CFWI is insensitive to the variation in the source strength, that is to differences in source strength between the observed and simulated data. When compared Fig. 11(b) with Fig. 9(d), it can be concluded that CFWI is still robust handling data contaminated by Gaussian white noise even in the case of variable source strength.

#### 4.4 Sensitivity of CFWI to source signature

In the previous section, we have operated with the true source wavelet and have seen that CFWI is insensitive to the source strength. In this section, we go beyond and investigate the

sensitivity of CFWI to the error in source signature. We use the Marmousi model (Fig. 6a) to synthesize two data sets named I and II with the two incorrect source wavelets shown in Fig. 2 (incorrect wavelets I and II), respectively. First, we invert these two data sets with the initial velocity model A and the data set I. The two frequency bands here considered are the previously listed in Section 4.1. The final inverted results are shown in Fig. 12. The left-hand column allows seeing the results obtained with the L2 norm, while the right-hand column allows seeing the results obtained with the normalized zero-lag cross-correlation function. The inverted results with the data set I simulated by the first incorrect source wavelet are shown in Figs 12(a) and (b). As the incorrect source wavelet I presents large side lobes and deviates clearly from the true wavelet, the inverted results obtained by the L2 norm (Fig. 12a) are now cycle skipped because the spurious wavelet acts to cause some arrivals to become incorrectly aligned between the observed and predicted data, despite the starting model is accurate. In contrast, CFWI inverts the basically outline of the faults in the Marmousi model (Fig. 12b). The MAPEs related to the inverted results represented in Figs 12(a) and (b) are 18.17 and 9.78 per cent, respectively, which further confirms that the inverted results obtained by CFWI are more accurate.

Then, the data set II simulated by the incorrect source wavelet II is also inverted. The results are shown in Figs 12(c) and (d). Despite this second incorrect wavelet is quite approximate to the true source wavelet except for smaller lobes, FWI with the L2 norm still converges to a local minimum. Unlike FWI with the L2 norm, CFWI can successfully invert the Marmousi model although with low resolution. The MAPEs related to the inverted results represented in Figs 12(c) and (d) are 8.54 and 5.87 per cent, respectively. Comparing the left-hand column to the right-hand column, it can be concluded that CFWI is more insensitive to the error in source signature. This can be attributed to the relaxation of the normalized zero-lag cross-correlation on amplitude matching.

Finally, a source estimation procedure (Groos *et al.* 2014) is also adopted at each iteration of FWI with the data set I simulated by the first incorrect source wavelet. In fact, this source estimation is about a Wiener deconvolution and at this point we recommend the readers going to the paper of Groos *et al.* (2014) for details. The results obtained by inversion with the data set I and the source estimation are shown in Figs 12(e) and (f). As can be seen these results yield well reconstructed structures with high resolution. The MAPEs related to the inverted results represented in Figs 12(e) and (f) are 3.71 and 4.13 per cent, which are even comparable with those obtained with noise-free data (see Section 4.1, Fig. 8). This illustrates that the effectiveness of this source inversion method. Because a source signature estimation includes not only the amplitude but also the phase, the normalized zero-lag cross-correlation function only is insensitive to the amplitude mismatch but not to the whole of the source signature. Therefore, an estimation of source signature is still needed to reconstruct models with high resolution when the source wavelet is severely erroneous.

#### 4.5 Sensitivity of CFWI to non-Gaussian white noise

As pointed by several other authors (Guitton & Symes 2003; Brossier *et al.* 2009, 2010; Ha *et al.* 2009), FWI with the L2 norm is insensitive to Gaussian white noise, but is sensitive to non-Gaussian white noise. In what follows, we test FWI with data that resemble strong ground motion and non-Gaussian noise.

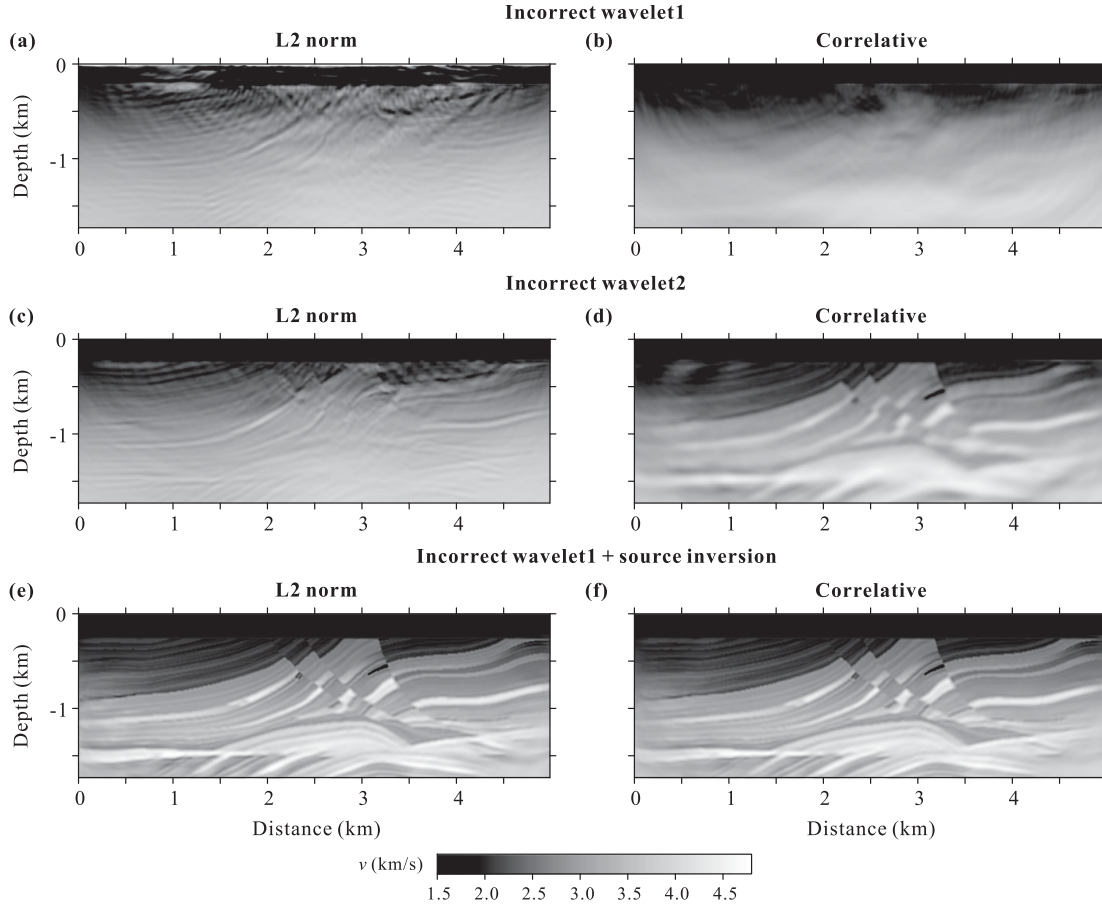


**Figure 12.** Multiscale images obtained using noise-free data simulated by the incorrect source wavelets (shown in Fig. 2) without and with source inversion. The initial model is shown in Fig. 6(b). The left-hand column are the final results obtained by the conventional L2 norm after iterations at the second frequency band, while the right-hand column are the final results obtained with the normalized zero-lag cross-correlation function after iterations at the same frequency band. The top two rows are the inverted results with noise-free data simulated by the incorrect source wavelets I and II (Fig. 2), respectively. The bottom row shows the inverted results with the noise-free data simulated by the incorrect source wavelet I, but employing a source estimation method at each iteration.

#### 4.5.1 Randomly rescaled traces

In this experiment, we randomly rescaled some seismic traces contaminated by Gaussian white noise (SNR equal to 20 dB, Fig. 7b) to simulate a poorly pre-processed strong ground motion data set. To determine how each trace is rescaled, a pseudorandom number drawn from the standard uniform distribution on the open interval  $(0, 1)$  is assigned to each trace. Then, any seismic trace is rescaled (multiplied) by a factor 20 wherever the assigned random number is greater than 0.95 (i.e. we rescale only 5 per cent of the traces). Fig. 13(a) shows a common shot gather of the 17th shot records (see Fig. 7b) generated from the Marmousi model (Fig. 6a), where some traces appear rescaled as mentioned. The normalized zero-lag cross-correlation function relaxes on the amplitude matching, so that it can tolerate wrong or unpredictable amplitude (in the observed data) that cannot be modelled by wavefield extrapolation operator. Thus, in order to compare with the performances both of the L2 norm and the normalized zero-lag cross-correlation function with the performance of the Huber norm as, which is known as its robustness (Djikpéssé & Tarantola 1999; Guitton & Symes 2003; Brossier *et al.* 2009, 2010; Ha *et al.* 2009; Pyun *et al.* 2009; Bulcão *et al.* 2013; Jimenez Tejero *et al.* 2014), we also invert all the previously rescaled traces with the Huber norm. As pointed by Brossier *et al.* (2010), the threshold value  $\varepsilon = 0.2 \text{ mean}(|d_{\text{obs}_i}|)$  for the Huber criterion is less sensitive to outliers in the data than the one indi-

cated by Guitton & Symes (2003) based on  $\max(|d_{\text{obs}_i}|)$ . Therefore, we adopt the threshold value  $\varepsilon = 0.2 \text{ mean}(|d_{\text{obs}_i}|)$  in FWI with the Huber norm.

The multiscale images obtained by FWI with the different objective functions and the two already mentioned frequency bands are shown in Fig. 14. From top to bottom, we display the inverted results with the L2 norm, the Huber norm and the normalized zero-lag cross-correlation function. From left-hand to right-hand side, we display the results inverted at the two frequency bands. Obviously, the models obtained with the L2 norm (top) suffer severe smearing, whereas FWI with either the Huber norm or the normalized zero-lag cross-correlation function inverts successfully the Marmousi model. Nevertheless, it can be easily observed that the results obtained with the Huber norm (middle) are comparatively noisier than the results obtained by CFWI (bottom). In particular, regarding the first frequency band, the model obtained with the Huber norm (Fig. 14c) looks somewhat noisy compared to the model obtained with the normalized zero-lag cross-correlation function (Fig. 14e). This same effect remains at the higher frequency band although it becomes weaker (Fig. 14d). This demonstrates that CFWI can suppress noise in the inversion process, which can be further explained by its adjoint source shown in Fig. 15. It can be observed that the adjoint source of the Huber norm (Fig. 15a) is clearly noisier in comparison with those of the normalized zero-lag cross-correlation function (Fig. 15b). These results illustrate that CFWI can

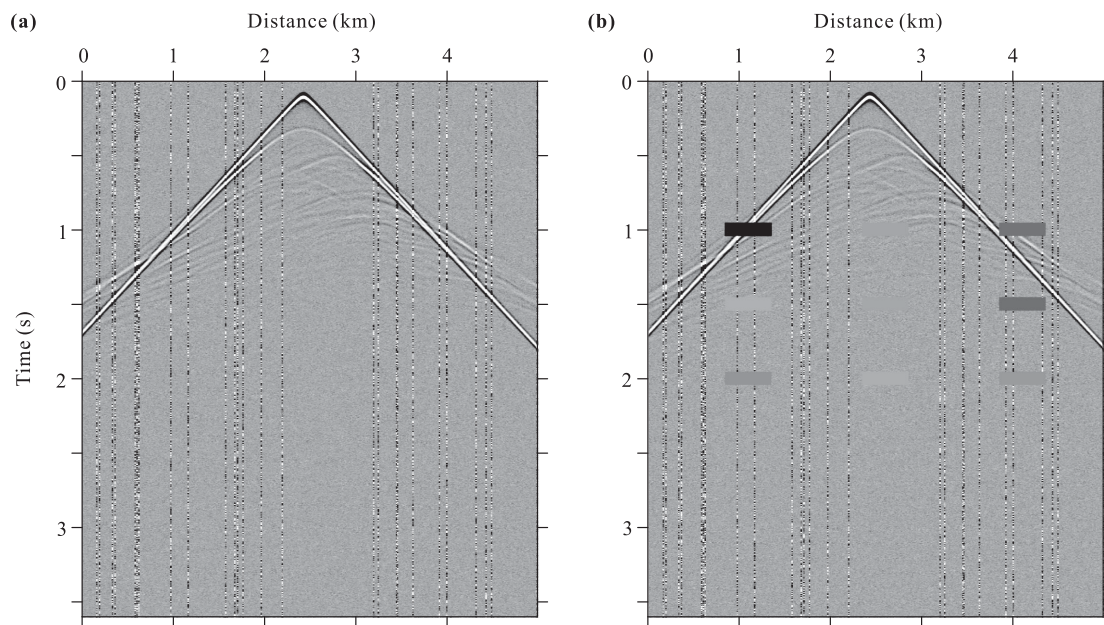


**Figure 13.** Common shot gathers of the 17th shot generated from the Marmousi model. Panel (a) shows the data contaminated by Gaussian white noise with the signal-to-noise ratio (SNR) of 20 dB, where the seismic traces have been randomly rescaled by a factor 20 to simulate strong ground motion. Panel (b) shows the data contaminated by non-Gaussian noise generated by adding up to nine rectangles in whose interior the data are first replaced by its average value and then rescaled by a factor 20.

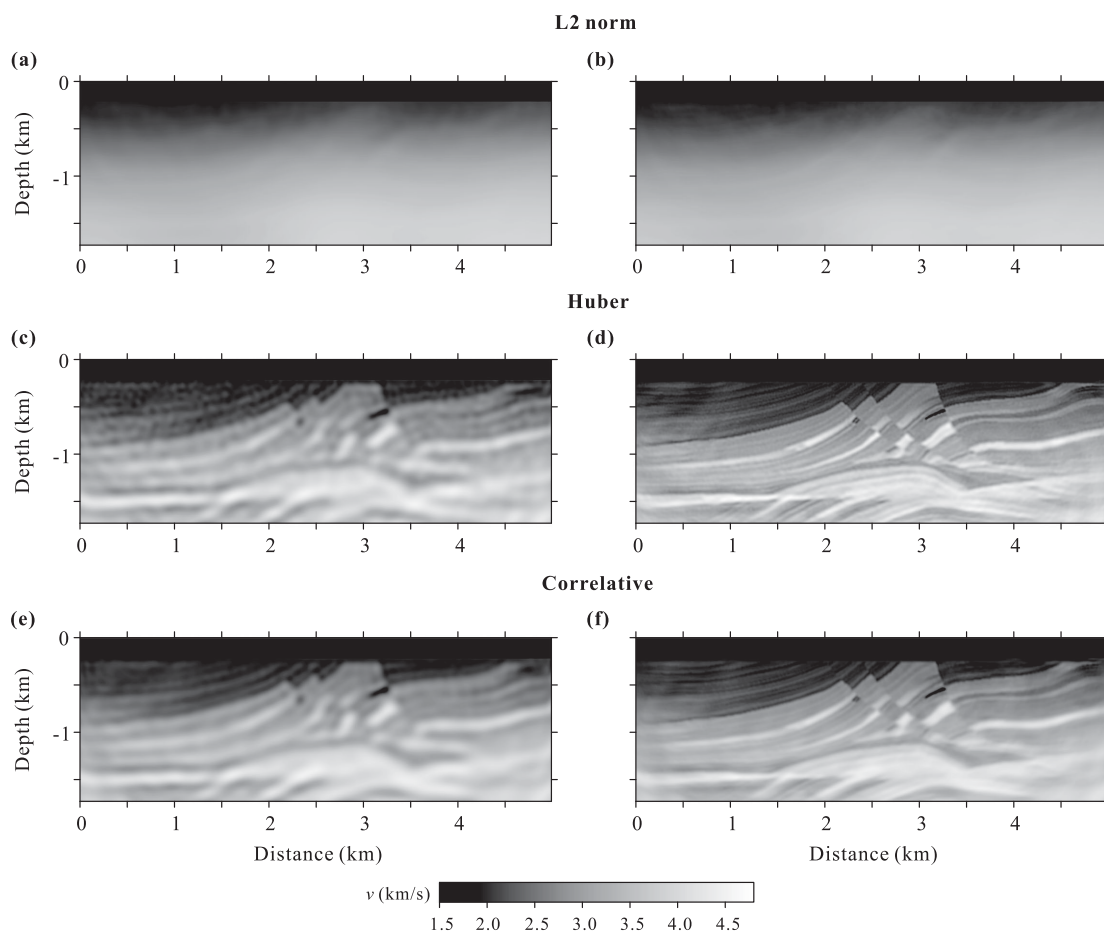


**Figure 14.** Multiscale images obtained by FWI with different objective functions. The initial model is shown in Fig. 6(b). From top to bottom, inverted results computed at two frequency bands with the L2 norm (a and b), the Huber norm (c and d) and the normalized zero-lag cross-correlation function (e and f). Here, the data is contaminated by Gaussian white noise (SNR equal to 20 dB) and some traces are rescaled by a factor 20 (Fig. 13a).

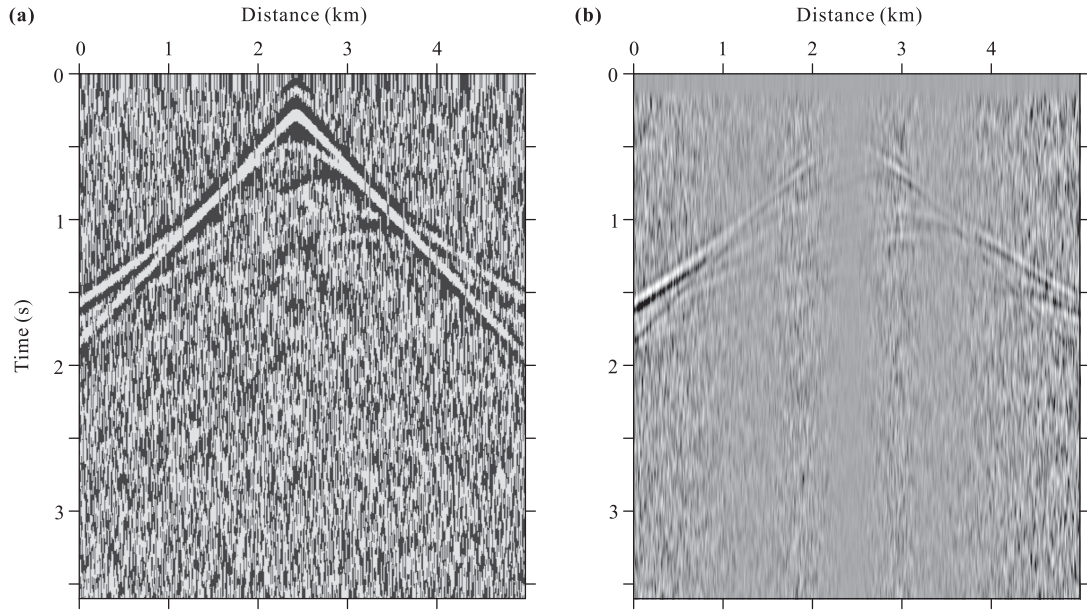


**Figure 15.** The initial adjoint sources of the 17th shot generated from the rescaled traces shot gathers (Fig. 13a) and different objective functions. Panel (a) shows the initial adjoint source obtained by the Huber norm, while panel (b) shows the initial adjoint source obtained by the normalized zero-lag cross-correlation function.

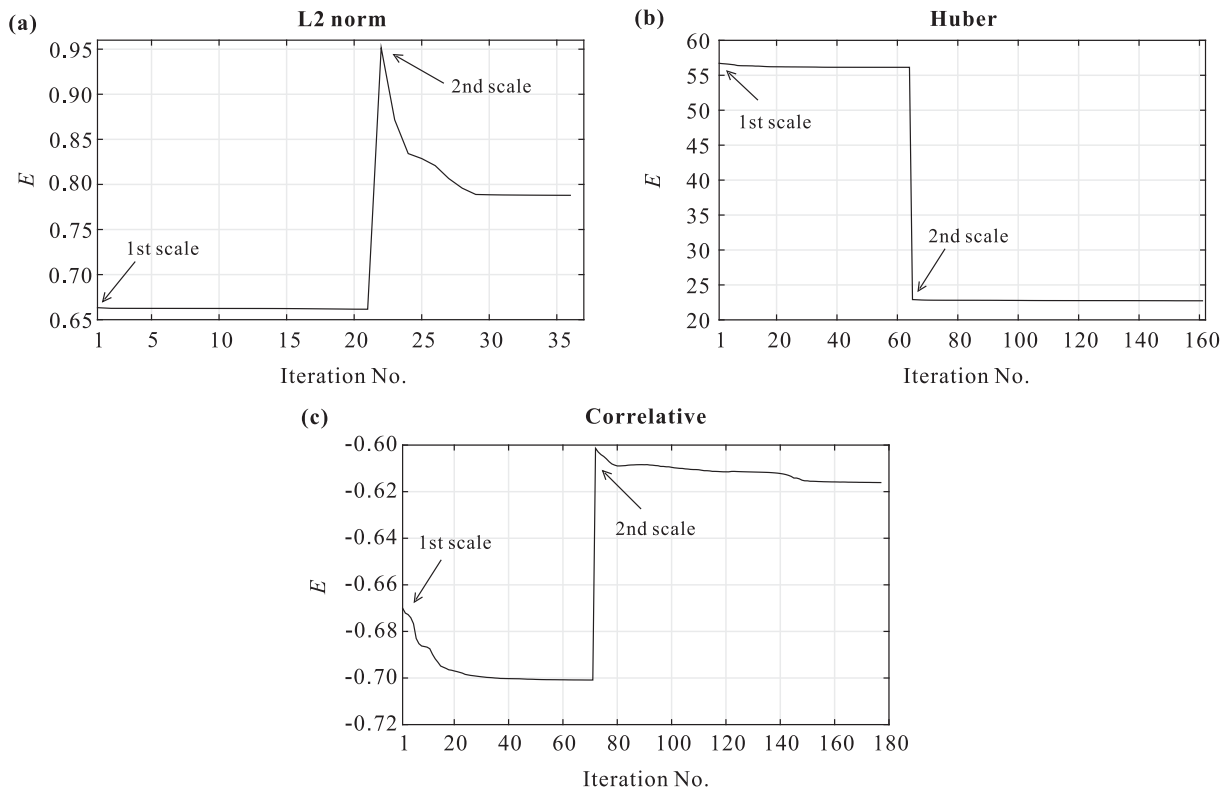


**Figure 16.** Objective function ( $E$ ) versus the number of iterations in relation to the multiscale images shown in Fig. 14, obtained with the starting velocity model shown in Fig. 6(a). The curves plotted are convergence curves obtained with the L2 norm (a), the Huber norm (b) and the normalized zero-lag cross-correlation function (c), respectively. Reference to the two frequency bands considered in this numerical example is done.

successfully invert data contaminated by randomly rescaled seismic traces (imitating strong ground motion noise). Besides, the MAPEs associated with the final results obtained by the L2 norm, the Huber norm and the normalized zero-lag cross-correlation function are 8.48, 4.77 and 5.06 per cent, respectively, which further confirms the robustness of CFWI to non-Gaussian noise.

In relation to the multiscale images shown in Fig. 14, obtained with the initial model A (Fig. 6b), the misfit function values versus the number of iterations are given in Fig. 16, where reference to the two frequency bands considered in this numerical example is done. The curves plotted are convergence curves obtained with the L2 norm (a), the Huber norm (b) and the normalized zero-lag

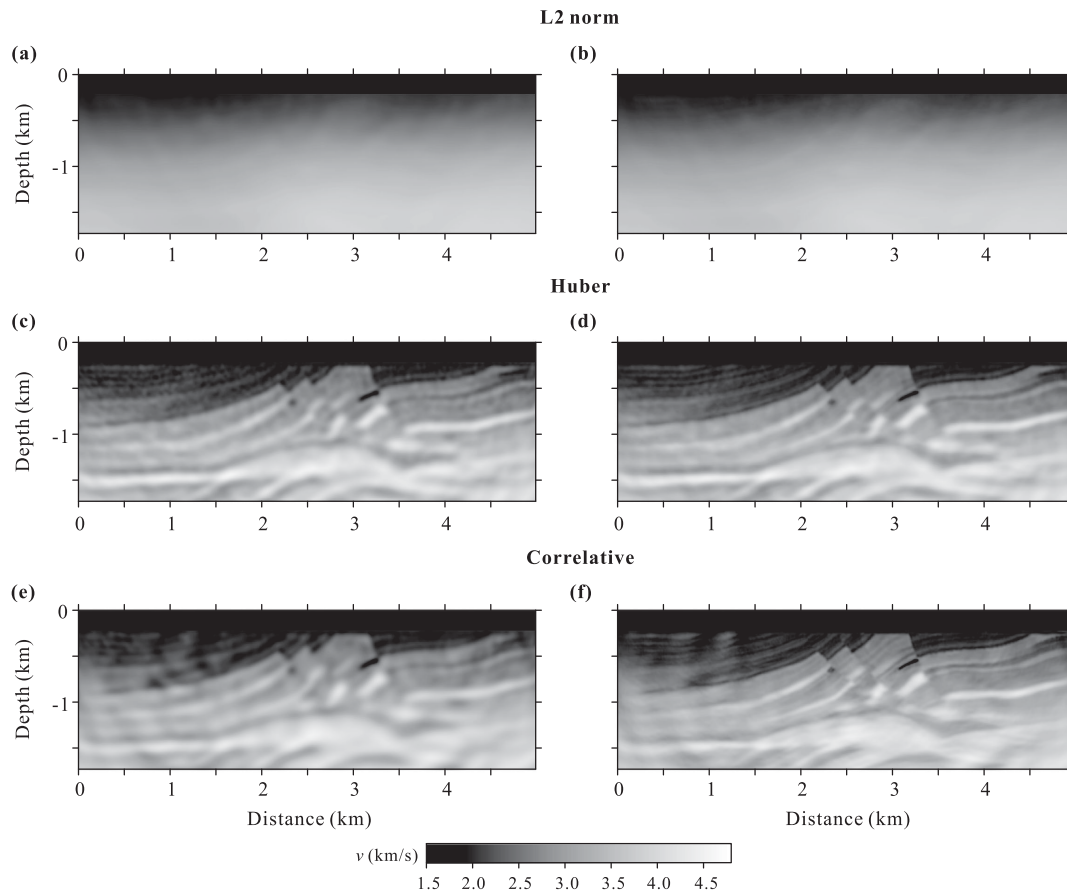


**Figure 17.** Same as in Fig. 14, using data contaminated by spike-type noise (Fig. 13b).

cross-correlation function (c). This demonstrates that FWI with any of these objective functions and applying the multiscale inversion is a convergent process instead of a divergent one (meets the predefined stopping criterion). Now then, the L2 norm is sensitive to randomly rescaled traces data. Compared to the Huber norm, CFWI can produce clearer images for randomly rescaled traces data that simulate poorly pre-processed strong ground motion data.

#### 4.5.2 Spike-type noise

To further test the sensitivity of CFWI to a more complex non-Gaussian noise scenario, we insert up to nine small rectangles (windows) on the shot gathers with rescaled traces such as the ones shown in Fig. 13(a). Inside each of these rectangles, synthetic data is first replaced by its average value within the time window and secondly is rescaled by a factor 20, thus simulating spike-type noise. The sizes and positions of the nine rectangles are fixed for all 34 shots. As an example, Fig. 13(b) shows the typically synthetic seismograms thus constructed for the 17th shot. We invert these shot gathers with the initial velocity model A and using the multiscale strategy.

The inverted results obtained by FWI with the L2 norm, the Huber norm, and the normalized zero-lag cross-correlation function, with data contaminated by spike-type noise, are shown in Fig. 17 from top to bottom. From left-hand to right-hand side, we display the results inverted at the two frequency bands listed in Section 4.1, respectively. Similar to the previous case, the resolution obtained with the L2 norm (Figs 17a and b) is fairly poor (Rao *et al.* 2006). As can be seen, both the Huber norm (Figs 17c and d) and the

normalized zero-lag cross-correlation function (Figs 17e and f) are able to successfully recover the Marmousi model and to produce comparable results, although both norms generally give rise to low-resolution images compared those represented in Fig. 15. However, in contrast with the normalized zero-lag cross-correlation function (Figs 17e and f), the results obtained by the Huber norm (Figs 17c and d) are noisier as we already have seen in the last section. It further indicates that CFWI can effectively suppress noise in the inversion process. In this numerical example, the MAPEs in correspondence with the three test functionals are 8.57, 5.73 and 5.84 per cent, respectively, which again demonstrates that the normalized zero-lag cross-correlation function is robust, compared to the Huber norm even with data contaminated by spike-type noise.

In relation to the multiscale images shown in Fig. 17, obtained with the initial velocity A (Fig. 6b) by FWI with the L2 norm, the Huber norm and the normalized zero-lag cross-correlation function, the misfit function values versus the number of iterations are given in Fig. 18, where reference to the two frequency bands considered in this numerical example is done (as before). The corresponding curves converge to the predefined stopping threshold. Once again, this demonstrates that FWI with any of these objective functions and applying the multiscale inversion is a convergent process instead of a divergent one.

## 5 SENSITIVITY OF CFWI TO CYCLE-SKIPPING

As we pointed in Section 3, the normalized zero-lag cross-correlation function seems to be more sensitive to the cycle-skipping

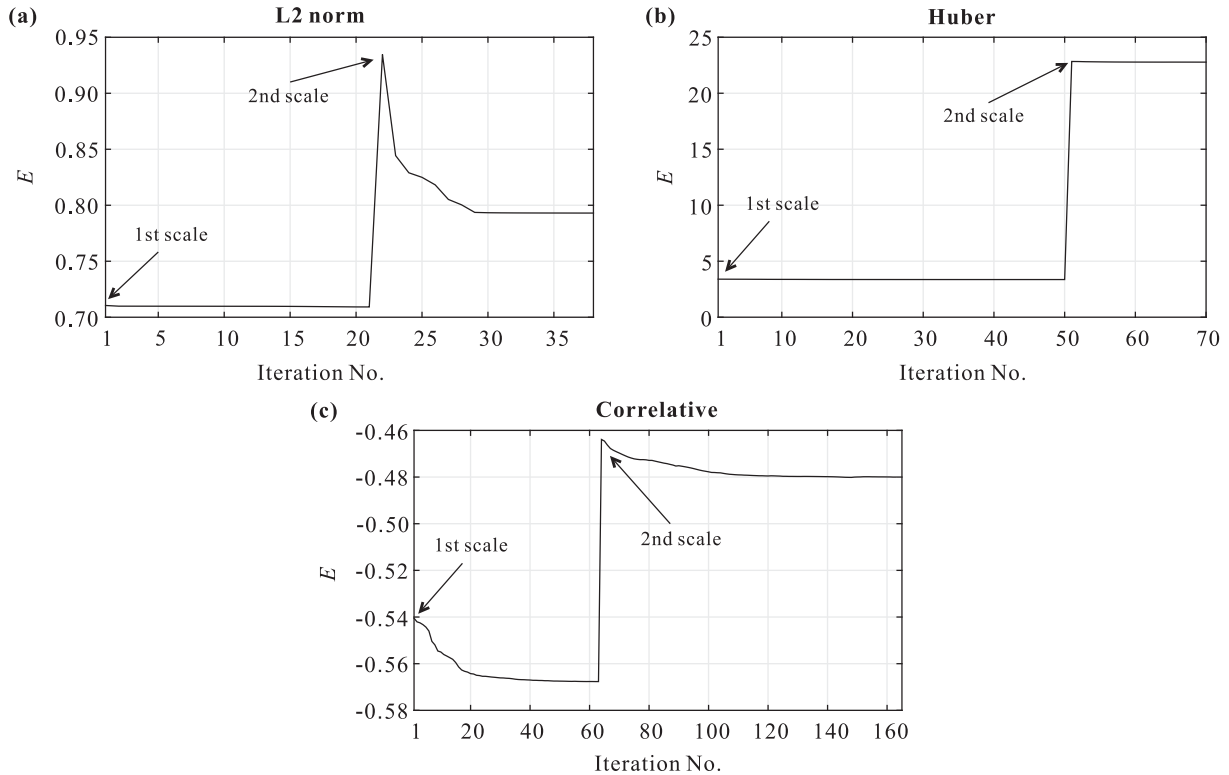


Figure 18. Same as in Fig. 16, using data contaminated by spike-type noise (Fig. 13b).

problem (i.e. the time difference between the observed and predicted data is greater than half a cycle) caused by less-accurate initial velocity model than the L2 norm. To investigate this issue, we consider the noise-free data from shot gathers generated with the Marmousi model (Fig. 6a), and start the inversions with the initial velocity model B (described in Section 4.1, Fig. 6c). Fig. 9(a) shows the observed (solid black lines) and predicted (dashed grey lines) data excited by the first shot (first cross in Fig. 6a) and recorded at the last receiver (the inverted triangle), while Fig. 19(b) shows the observed (solid black lines) and predicted data (dashed grey lines) excited by the 17th shot (second cross to the right-hand side in Fig. 6a) and recorded at the same receiver. The two plots contain both the head wave and direct wave. In Fig. 19(a), the predicted head wave advances almost 111 ms with respect to the observed head wave, which is less than half a cycle, that is 254 ms. In Fig. 19(b), the predicted head wave delay almost 74 ms with respect to the observed head wave, which is also less than half a cycle, that is 203 ms. This demonstrates that the predicted data generated by the initial model B is free from the cycle-skipping problem.

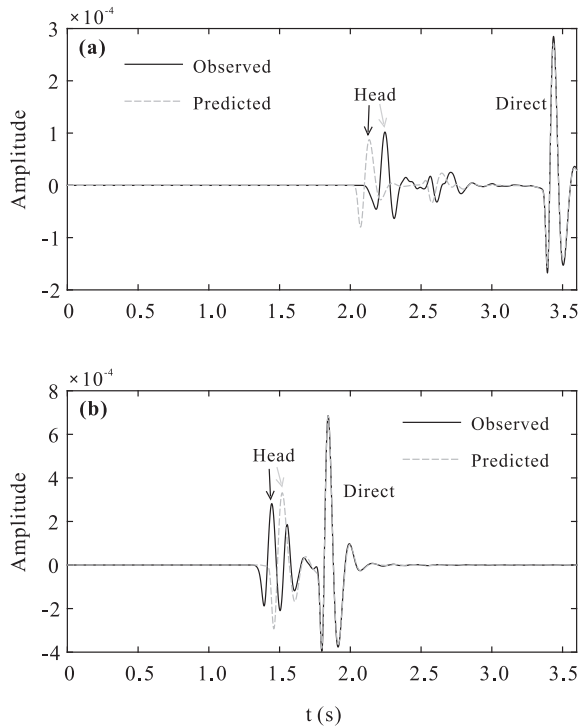
We use the multiscale strategy (Section 4.1) to invert the noise-free data using the initial model B. In order to check whether the normalized zero-lag cross-correlation function is sensitive to the cycle-skipping problem, we also invert the noise-free data with the L2 norm for a comparison. Fig. 20 shows the multiscale images obtained using noise-free data (Fig. 7a) and these different objective functions. From left to right we display the inverted results obtained with the L2 norm and the normalized zero-lag cross-correlation, while from top to bottom we display the results inverted at the two frequency bands. Theoretically, since the predicted data generated by the initial model B is free from cycle-skipping, both the L2 norm and the normalized zero-lag cross-correlation function should obtain high-resolution models as those shown in

Fig. 8. Unfortunately, the models obtained by the normalized zero-lag cross-correlation function (right-hand column in Fig. 20) suffer smearing at the two frequency bands, whereas FWI with the L2 norm provides almost comparable high-resolution results to those inverted using the initial model A (Figs 8a and b). This is consistent with the conclusion drawn in Section 3 (Fig. 3). The MAPEs corresponding to the inverted results shown in Fig. 20 are 5.94 and 6.35 per cent, respectively. This confirms that the normalized zero-lag cross-correlation function is more sensitive to the cycle-skipping problem caused by less-accurate initial model.

## 6 CONCLUSIONS

We have implemented FWI with a distinct objective function that maximizes the minus normalized zero-lag cross-correlation between the observed and simulated data for FWI. The method, that we call CFWI, is similar to FWI with the L2 norm, and at the same time whose robustness is free of a threshold criterion that controls the transition between the L2 and L1 norms used in the Huber and Hybrid norms. Because the normalized zero-lag cross-correlation function relaxes on the amplitude matching and emphasizes the phase information, it can tolerate wrong amplitude in the observed data that cannot be predicted by the wavefield extrapolation operator. Consequently, it is expected that this method is insensitive to wrong amplitude or to noise in benefit of its further application. Several numerical experiments support the effectiveness, robustness and sensitivity of CFWI. The effectiveness of CFWI is clear since it allows to recover the Marmousi model with a resolution comparable to that of other norms, even with data contaminated by Gaussian white noise.

In practice, the accurate estimation of the seismic source strength is difficult so that the amplitude matching achieved by FWI with



**Figure 19.** The observed (solid black lines) and predicted (dashed grey lines) data excited by the two shots shown in Fig. 6 and recorded at the last receiver (the triangle). The plot (a) shows the data from the first shot, while the plot (b) shows the data from the 17th shot. The head and direct waves are indicated in both plots.

the L2 norm is never perfect. On the contrary, CFWI is insensitive to differences in the source strength. FWI with the L2 norm fails to invert the rescaled shot gathers without appropriate data pre-processing, however FWI with the normalized zero-lag cross-correlation function is able to invert these shot gathers successfully. Moreover, the normalized zero-lag cross-correlation function is slightly more insensitive to the source signature than the L2 norm.

The L2 norm leads to a spurious model even when the assumed source wavelet is slightly erroneous, whereas the normalized zero-lag cross-correlation function can obtain a low-resolution result. Nevertheless, an estimation of seismic signature is also necessary to achieve a high-resolution result when the source signature is severely erroneous. This is because the seismic source estimation involves both the amplitude and phase of seismic wavelet.

When testing the sensitivity of CFWI against data contaminated by non-Gaussian noise, the results obtained with the Huber norm and the normalized zero-lag cross-correlation function are fully comparable and both norms give rise to high-resolution images. CFWI is insensitive to both Gaussian noise and non-Gaussian white noise. This can be attributed to the fact that the normalized zero-lag cross-correlation function is equivalent to a time-domain phase inversion method where the phase spectra of the simulated data are matched with those of the observed data. CFWI reduces the importance of the amplitude and provides a basis for using the phase information to measure the closeness between the observed and simulated seismic data. Therefore, it is an alternative inversion algorithm that can be used to deal with data contaminated by non-Gaussian noise. In particular, it can suppress the noise in data to generate clear images when compared with the Huber norm.

Finally, even though the predicted data generated by an initial model to be free from the cycle-skipping problem, the fact is that the normalized zero-lag cross-correlation function converges to a low-resolution result, which confirms that it is comparatively more sensitive to the cycle-skipping problem caused by less-accurate initial model.

## ACKNOWLEDGEMENTS

We want to remember Prof Zhongjie Zhang, who was the leader of the research group in the Institute of Geology and Geophysics of Chinese Academy of Sciences (IGGCAS) and also our dear friend, who unexpectedly passed away on September 6th, 2013. The authors are thankful to the Computer Simulation Laboratory

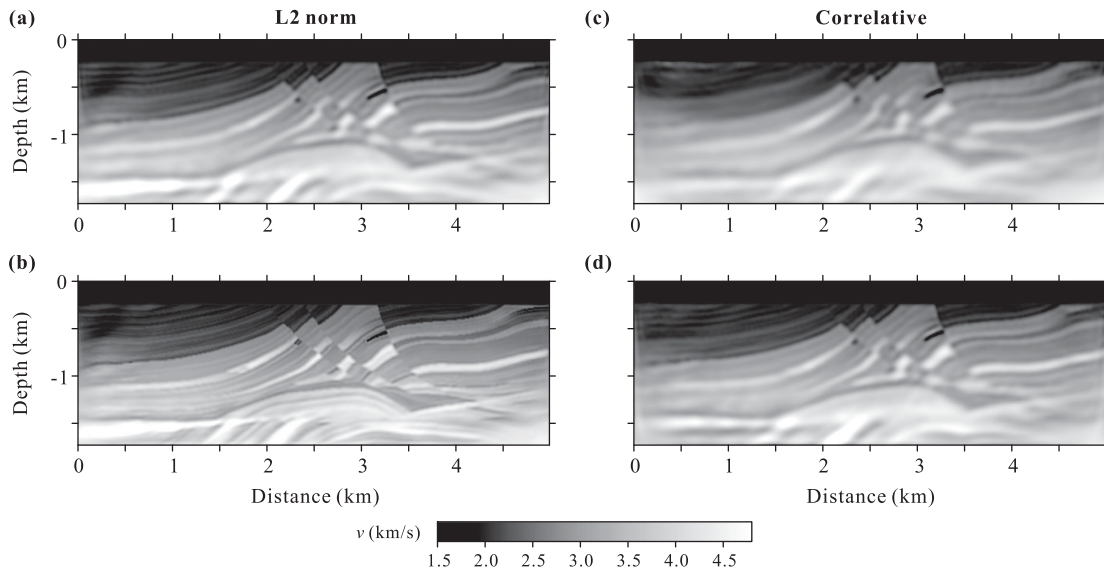


**Figure 20.** Multiscale images obtained using noise-free data (Fig. 7a) and two different objective functions. The initial model is shown in Fig. 6(c). The left-hand column shows the results obtained by the conventional L2 norm at two frequency bands (from low to high frequency bands, a and b), while the right-hand column shows the results obtained with the normalized zero-lag cross-correlation function at the same frequency bands (from low to high frequency bands, c and d).

of IGGCAS for allocation of computing time. We are very thankful to Dr Daniel Köhn, who provided us with the Marmousi model (Fig. 6a) and the initial model A (Fig. 6b) obtained by the first-arrival traveltimes tomography based on the adjoint-state method, and gave us helpful suggestions. We are also very grateful to Jinhai Zhang for his generous assistance in computation tasks and the facilities given in the course of this work. We thank the constructive discussions with Qiancheng Liu and Xuejian Liu. We also appreciate the useful comments from Assistant Editors Prof Jean Virieux and Dr René-Edouard Plessix and an anonymous reviewer, all of them contributed to substantially improve the early manuscript and made possible a better presentation of this paper. We gratefully acknowledge the financial support for this work contributed by the National key research and development program of China (grant no. 2016YFC0600101, 2016YFC0600201), the National Natural Science Foundation of China (grants no. 41604076, 41674102, 41674095, 41522401, 41374062, 41274070, 41404073), the China Earthquake Administration (grant no. 201408023) and the first class general financial grant from China Postdoctoral Science Foundation (grant no. 2016M600128).

## REFERENCES

- Alkhalifah, T. & Choi, Y., 2014. From tomography to full-waveform inversion with a single objective function, *Geophysics*, **79**, R55–R61.
- Bednar, J., Shin, C. & Pyun, S., 2007. Comparison of waveform inversion, Part 2: Phase approach, *Geophys. Prospect.*, **55**, 465–475.
- Boonyasiriwat, C., Valasek, P., Routh, P., Cao, W., Schuster, G.T. & Macy, B., 2009. An efficient multiscale method for time-domain waveform tomography, *Geophysics*, **74**, WCC59–WCC68.
- Bozdag, E., Trampert, J. & Tromp, J., 2011. Misfit functions for full waveform inversion based on instantaneous phase and envelope measurements, *Geophys. J. Int.*, **185**, 845–870.
- Brenders, A., Pratt, R. & Charles, S., 2009. Waveform tomography of 2-D seismic data in the Canadian foothills—data preconditioning by exponential time-damping, in *Proceedings of the 71st Annual International Conference and Exhibition*, EAGE, Extended Abstracts, U041.
- Brethaudou, F., Brossier, R., Métivier, L. & Virieux, J., 2014. First-arrival delayed tomography using 1st and 2nd order adjoint-state method, in *Proceedings of the 84th Annual International Meeting*, SEG, Expanded Abstracts, pp. 4757–4761.
- Brossier, R., Operto, S. & Virieux, J., 2009. Robust elastic frequency-domain full-waveform inversion using the  $L_1$  norm, *Geophys. Res. Lett.*, **36**, L20310, doi:10.1029/2009GL039458.
- Brossier, R., Operto, S. & Virieux, J., 2010. Which data residual norm for robust elastic frequency-domain waveform inversion?, *Geophysics*, **75**, R37–R46.
- Bube, K.P. & Langan, R.T., 1997. Hybrid  $L_1/L_2$  minimization with applications to tomography, *Geophysics*, **62**, 1183–1195.
- Bulcão, A., Soares Filho, S., Loureiro, D.M., Alves, F.P., Farias, G.C., Santos, F.F. & Petrobras, L.A., 2013. Full waveform inversion: comparison between different objective functionals, in *Proceedings of the 13th International Congress of the Brazilian Geophysical Society & EXPOGEE*, Rio de Janeiro, Brazil, 2013 August 26–29.
- Bunks, C., Saleck, F.M., Zaleski, S. & Chavent, G., 1995. Multiscale seismic waveform inversion, *Geophysics*, **60**, 1457–1473.
- Causse, E., Mittet, R. & Ursin, B., 1999. Preconditioning of full-waveform inversion in viscoacoustic media, *Geophysics*, **64**, 130–145.
- Chen, P., Jordan, T. & Zhao, L., 2007. Full three-dimensional tomography: a comparison between the scattering-integral and adjoint-wavefield methods, *Geophys. J. Int.*, **170**, 175–181.
- Chi, B., Dong, L. & Liu, Y., 2014. Full waveform inversion method using envelope objective function without low frequency data, *J. appl. Geophys.*, **109**, 36–46.
- Choi, Y. & Alkhalifah, T., 2012. Application of multi-source waveform inversion to marine streamer data using the global correlation norm, *Geophys. Prospect.*, **60**, 748–758.
- Cruse, E., Pica, A., Noble, M., McDonald, J. & Tarantola, A., 1990. Robust elastic nonlinear waveform inversion: application to real data, *Geophysics*, **55**, 527–538.
- de Hoop, M.V. & van der Hilst, R.D., 2005. On sensitivity kernels for ‘wave equation’ transmission tomography, *Geophys. J. Int.*, **160**, 621–633.
- Djikpéssé, H.A. & Tarantola, A., 1999. Multiparameter  $l_1$  norm waveform fitting: interpretation of Gulf of Mexico reflection seismograms, *Geophysics*, **64**, 1023–1035.
- Dutta, G., Sinha, M. & Schuster, G.T., 2014. A cross-correlation objective function for least-squares migration and visco-acoustic imaging, in *Proceedings of the 84th Annual International Meeting*, SEG, Expanded Abstracts, pp. 3980–3990.
- Fichtner, A., 2010. *Full Seismic Waveform Modelling and Inversion*, Springer-Verlag.
- Fichtner, A., Kennett, B.L.N., Igel, H. & Bunge, H., 2008. Theoretical background for continental- and global-scale full-waveform inversion in the time-frequency domain, *Geophys. J. Int.*, **175**, 665–685.
- Fichtner, A., Trampert, J., Cupillard, P., Saygin, E., Taymaz, T., Capdeville, Y. & Villaseñor, A., 2013. Multiscale full waveform inversion, *Geophys. J. Int.*, **194**, 534–556.
- Groos, L., Schäfer, M., Forbriger, T. & Bohlen, T., 2014. The role of attenuation in 2D full-waveform inversion of shallow-seismic body and Rayleigh waves, *Geophysics*, **79**, R247–R261.
- Guitton, A., 2012. Blocky regularization schemes for full waveform inversion, *Geophys. Prospect.*, **60**, 870–884.
- Guitton, A. & Symes, W.W., 2003. Robust inversion of seismic data using the Huber norm, *Geophysics*, **68**, 1310–1319.
- Ha, T., Chung, W. & Shin, C., 2009. Waveform inversion using a back-propagation algorithm and a Huber function norm, *Geophysics*, **74**, R15–R24.
- Hale, D., 2013. Dynamic warping of seismic images, *Geophysics*, **78**, S105–S115.
- Hörmann, G. & de Hoop, M.V., 2002. Detection of wave front set perturbations via correlation: foundation for wave-equation tomography, *Appl. Anal.*, **81**, 1443–1465.
- Huang, J.-W. & Belleur, G., 2012. Joint transmission and reflection traveltime tomography using the fast sweeping method and the adjoint-state technique, *Geophys. J. Int.*, **188**, 570–582.
- Huber, P.J., 1973. Robust regression: asymptotics, conjectures, and Monte Carlo, *Ann Stat.*, **1**, 799–821.
- Jimenez Tejero, C.E., Dagnino, D., Sallares, V. & Ranero, C., 2014. Comparison of objective functionals in seismic full waveform inversion, in *Proceedings of the 76th EAGE Conference & Exhibition 2014 Amsterdam RAI*, The Netherlands, 2014 June 16–19.
- Kim, W. & Shin, C., 2005. Phase inversion of seismic data with unknown source wavelet: synthetic examples, in *Proceedings of the 75th Annual International Meeting*, SEG, Expanded Abstracts, pp. 1685–1688.
- Kurzmann, A., 2012. Applications of 2D and 3D full waveform tomography in acoustic and viscoacoustic complex media, *PhD thesis*, Karlsruhe Institute of Technology (KIT). Available at: <http://nbn-resolving.de/urn:nbn:de:swb:90-344211>.
- Kvoren, Z., Mosegaard, K., Landa, E., Thore, P. & Tarantola, A., 1991. Monte Carlo estimation and resolution analysis of seismic background velocities, *J. geophys. Res.*, **96**, 20 289–20 299.
- Lailly, P., 1983. The seismic inverse problems as a sequence of before stack migration, in *Proceedings of the Conference on Inverse Scattering Theory and Application*, Society of Industrial and Applied Mathematics, pp. 206–220.
- Leung, S. & Qian, J., 2006. An adjoint state method for three-dimensional transmission traveltimes tomography using first-arrivals, *Commun. Math. Sci.*, **4**, 249–266.
- Liu, Q. & Gu, Y., 2012. Seismic imaging: from classical to adjoint tomography, *Tectonophysics*, **566–567**, 31–66.
- Liu, Q. & Tromp, J., 2006. Finite-frequency kernels based on adjoint methods, *Bull. seism. Soc. Am.*, **96**, 2383–2397.

- Liu, Q. & Tromp, J., 2008. Finite-frequency sensitivity kernels for global seismic wave propagation based upon adjoint methods, *Geophys. J. Int.*, **174**, 265–286.
- Liu, Y., Liu, S., Zhang, M. & Ma, D., 2012. An improved perfectly matched layer absorbing boundary condition for second order elastic wave equation (in Chinese), *Prog. Geophys.*, **27**, 2113–2122.
- Liu, Y., Teng, J., Xu, T. & Badal, J., 2017. Analysis of factors influencing the multiscale full waveform inversion in time-domain, *Pure appl. Geophys.*, in press.
- Luo, Y. & Schuster, G., 1991. Wave-equation traveltimes inversion, *Geophysics*, **56**, 645–653.
- Luo, J. & Wu, R., 2015. Seismic envelope inversion: reduction of local minima and noise resistance, *Geophys. Prospect.*, **63**, 597–614.
- Mora, P.R., 1987. Nonlinear two-dimensional elastic inversion of multioffset seismic data, *Geophysics*, **52**, 1211–1228.
- Mosegaard, K. & Tarantola, A., 1995. Monte Carlo sampling of solutions to inverse problems, *J. geophys. Res.*, **100**, 12 431–12 447.
- Nocedal, J., 1980. Updating quasi-Newton matrices with limited storage, *Math. Comput.*, **95**, 339–353.
- Operto, S., Virieux, J., Amestoy, P., L'Excellent, J., Giraud, L. & Ali, J.B.H., 2007. 3D finite-difference frequency-domain modeling of visco-acoustic wave propagation using a massively parallel direct solver: a feasibility study, *Geophysics*, **72**, SM195–SM211.
- Plessix, R.E., 2006. A review of the adjoint-state method for computing the gradient of a functional with geophysical applications, *Geophys. J. Int.*, **167**, 495–503.
- Plessix, R.E., Baeten, G., de Maag, J.W., Klaassen, M., Zhang, R. & Tao, Z., 2010. Application of acoustic full waveform inversion to a low-frequency large-offset land data set, *SEG, Expanded Abstracts*, **29**, 930–934.
- Pratt, R.G., 1990. Inverse theory applied to multi-source cross-hole tomography—Part I: Acoustic wave-equation method, *Geophys. Prospect.*, **39**, 287–310.
- Pratt, R.G. & Gouly, N.R., 1991. Combining wave-equation imaging with traveltimes tomography to form high-resolution images from crosshole data, *Geophysics*, **56**, 208–224.
- Pratt, R.G., Shin, C. & Hicks, G.J., 1998. Gauss-Newton and full Newton methods in frequency-space seismic waveform inversion, *Geophys. J. Int.*, **133**, 341–362.
- Pratt, R.G., Song, Z., Williamson, P. & Warner, M., 1996. Two-dimensional velocity models from wide-angle seismic data by wavefield inversion, *Geophys. J. Int.*, **124**, 323–340.
- Pyun, S., Shin, C. & Son, W., 2009. Frequency-domain waveform inversion using an L1-norm objective function, in *Proceedings of the 71st Conference & Exhibition, EAGE, Extended Abstracts*, P005.
- Rao, Y., Wang, Y. & Morgan, J.V., 2006. Crosshole seismic waveform tomography. II: Resolution analysis, *Geophys. J. Int.*, **166**, 1237–1248.
- Ravaut, C., Operto, S., Improta, L., Virieux, J., Herrero, A. & dell'Aversana, P., 2004. Multiscale imaging of complex structures from multifold wide-aperture seismic data by frequency-domain full-wavefield inversions: application to a thrust belt, *Geophys. J. Int.*, **159**, 1032–1056.
- Rothman, D., 1985. Nonlinear inversion, statistical mechanics, and residual statics estimation, *Geophysics*, **50**, 2784–2796.
- Routh, P. et al., 2011a. Full-wavefield inversion of marine streamer data with the encoded simultaneous source method, in *Proceedings of the Expanded Abstracts, 73th Annual Meeting, EAGE*.
- Routh, P. et al., 2011b. Encoded simultaneous source full-wavefield inversion for spectrally shaped marine streamer data, *SEG Technical Program Expanded Abstracts 2011*, **30**, 2433–2438.
- Schuster, G., 1991. Wave equation phase inversion in the frequency domain, in *Proceedings of the 61st Annual International Meeting, SEG, Expanded Abstracts*, pp. 909–912.
- Sheng, J., Leeds, A., Buddensiek, M. & Schuster, G.T., 2006. Early arrival waveform tomography on near-surface refraction data, *Geophysics*, **71**, U47–U57.
- Shin, C. & Cha, Y., 2008. Waveform inversion in the Laplace domain, *Geophys. J. Int.*, **173**, 922–931.
- Shin, C. & Ha, W., 2008. A comparison between the behavior of objective functions for waveform inversion in the frequency and Laplace domains, *Geophysics*, **73**, VE119–VE133.
- Shin, C. & Min, D.J., 2006. Waveform inversion using a logarithmic wavefield, *Geophysics*, **71**, R31–R42.
- Shipp, R.M. & Singh, S.C., 2002. Two-dimensional full wavefield inversion of wide-aperture marine seismic streamer data, *Geophys. J. Int.*, **151**, 325–344.
- Sirgue, L. & Pratt, R.G., 2004. Efficient waveform inversion and imaging: a strategy for selecting temporal frequencies, *Geophysics*, **69**, 231–248.
- Sun, Y. & Schuster, G.T., 1993. Time domain phase inversion, in *Proceedings of the 63rd Annual International Meeting, SEG, Expanded Abstracts*, pp. 684–687.
- Taillandier, C., Noble, M., Chauris, H. & Calandra, H., 2009. First-arrival traveltimes tomography based on the adjoint-state method, *Geophysics*, **74**, WCB1–WCB10.
- Tape, C., Liu, Q., Maggi, A. & Tromp, J., 2009. Seismic tomography of the southern California crust based on spectral-element and adjoint methods, *Geophys. J. Int.*, **180**, 433–462.
- Tarantola, A., 1984. Inversion of seismic reflection data in the acoustic approximation, *Geophysics*, **49**, 1259–1266.
- ten Kroode, F., Bergler, S., Corsten, C., de Maag, J.W., Strijbos, F. & Tijhof, H., 2013. Broadband seismic data—the importance of low frequencies, *Geophysics*, **78**, WA3–WA14.
- Tromp, J., Tape, C. & Liu, Q., 2005. Seismic tomography, adjoint methods, time reversal and banana-doughnut kernels, *Geophys. J. Int.*, **160**, 195–216.
- van Leeuwen, T. & Mulder, W.A., 2010. A correlation-based misfit criterion for wave-equation traveltimes tomography, *Geophys. J. Int.*, **182**, 1383–1394.
- Vigh, D., Starr, W. & Kapoor, J., 2009. Developing earth models with full waveform inversion, *Leading Edge*, **28**, 432–435.
- Wang, Y., 2011. Seismic waveform modeling and tomography, in *Encyclopaedia of Solid Earth Geophysics*, pp. 1290–1301, ed. Gupta, H.K., Springer Verlag.
- Wang, Y. & Pratt, R.G., 1997. Sensitivities of seismic traveltimes and amplitudes in reflection tomography, *Geophys. J. Int.*, **131**, 618–642.
- Wang, Y. & Rao, Y., 2006. Crosshole seismic waveform tomography I: Strategy for real data application, *Geophys. J. Int.*, **166**, 1224–1236.
- Wang, Y. & Rao, Y., 2009. Reflection seismic waveform tomography, *J. geophys. Res.*, **114**, doi:10.1029/2008JB005916.
- Warner, M. & Guasch, L., 2016. Adaptive waveform inversion: theory, *Geophysics*, **81**, R429–445.
- Wu, R., Luo, J. & Wu, B., 2014. Seismic envelope inversion and modulation signal model, *Geophysics*, **79**, WA13–WA24.
- Zhang, Y., Duan, L. & Xie, Y., 2013. A stable and practical implementation of least-squares reverse time migration, in *Proceedings of the 83rd Annual International Meeting, SEG, Expanded Abstracts*, pp. 3716–3720.
- Zhang, Y., Duan, L. & Xie, Y., 2015. A stable and practical implementation of least-squares reverse time migration, *Geophysics*, **80**, V23–V31.